Naval Research Laboratory

Washington, DC 20375-5320

NRL/FR/8121--93-9531

Ultraviolet Plume Instrument Description and Plume Data Reduction Methodology

H.W. SMATHERS
D.M. HORAN

Space Systems Development Department
Naval Center for Space Technology

J.G. CARDON
E.R. MALARET

Applied Coherent Technology Corporation
Herndon, Virginia

M.R. CORSON
J.E. BRANDENBURG

Research Support Instruments
Alexandria, Virginia

May 12, 1993

CONTENTS

FIGURES

TABLES

EXECUTIVE SUMMARY

The Ultraviolet Plume Instrument (UVPI) is a small, plume-tracking instrument flown on the Naval Research Laboratory's Low-power Atmospheric Compensation Experiment (LACE) satellite, which was launched on 14 February 1990. The UVPI's mission is to collect images of rocket plumes. Missile tracking in the ultraviolet range is advantageous because of extremely low Earth and solar backgrounds, extremely sensitive photodetectors that do not require cryogenic cooling, and very high optical resolution, which is possible with optics of relatively modest size. Because of missile tracking requirements, UVPI also has been used to collect background image data of Earth, Earth's limb, and celestial objects in the near and middle ultraviolet wavebands. Five rocket firings were observed. Background object imagery already collected with the UVPI includes the day and night Earth limb air glow, aurora, sunlit and moonlit clouds, solid Earth scenes with varying solar illumination, cities, and stars.

Typical UVPI observations range from 3 to 10 minutes and usually include between 2,000 and 5,000 images. Data are channeled to the UVPI Mission Planning and Assessment Center in Alexandria, Virginia, for processing and evaluation. More than over 200 observations were logged in two years of operation. Data tapes are archived in the Strategic Defense Initiative Organization (SDIO) Background Data Center at the Naval Research Laboratory (NRL) for further distribution. Data are acquired by two cameras, a tracker camera and a plume camera.

The UVPI system aperture is only 10 cm in diameter. However, it can detect and image missile plumes at 500 km range. The two cameras of the instrument use narrowband filters, image intensifiers, and charge-coupled devices (CCDs) to observe sources in the ultraviolet. The primary function of the tracker camera, viewing over a relatively wide field (1.98° by 2.60°) and broad spectrum [255 to 450 nanometers (nm)] is to locate and track a source for higher resolution observation by the plume camera. Images over this full field of view can be recorded at a 5 Hz image rate. The tracker camera can also be operated in a mode where the transmitted field of view is restricted to the central 17% of the full field of view, and the image rate is increased to 30 Hz. The plume camera has a narrow field of view (0.184° by 0.137°) and observes sources through any of four filters with passbands of 195 to 295 nm, 220 to 320 nm, 235 to 350 nm, and 300 to 320 nm. The wavelengths shorter than 310 nm are essentially invisible from the ground because of atmospheric absorption. Like the tracker camera, the plume camera can also be operated in a mode where the transmitted field of view is restricted to the central 17% of the full field of view, and the image rate is increased to 30 Hz. The limiting resolution of the tracker camera is about 230 μradians (μrad) and that of the plume camera about 90 μrad, equivalent at 500 km range to 115 m and 45 m, respectively.

In typical operation, the UVPI is programmed via ground command to point at the expected location of the plume or other object of interest. UVPI then enters a selected scan pattern until the desired object enters the field of view of the tracker camera. The tracker camera and control electronics on board UVPI then track the object, and both cameras gather image and radiometric data. The plume camera filter can be changed as desired during this data collection to select wavelength bandpasses. If the plume or object of interest is temporarily lost as a result of a coasting phase between rocket stages or some other reason, UVPI can be commanded to enter various extrapolation or search modes as required.

The UVPI is typically used to observe missiles in flight above the atmosphere. Therefore, stages of rockets fired at low altitude (below 20 km) are not expected to be visible in the ultraviolet from space. Rocket stages reaching 110-km altitude have been successfully detected and tracked by the UVPI from a range of 450 to 550 km for about 30 s. During these tests, approximately 500 $^1/_{30}$th-second images of plume data were acquired using the four plume-camera filters. The tracking of the plumes was of sufficient quality to permit the superposition of images for plume radiance

determination. Image superposition to enhance the signal level is needed for accurate radiometry because of the small telescope aperture.

The spectral radiance and spectral radiant intensities of the missile plumes were extracted from these images. Absolute values were obtained from an assumed spectral shape that was derived from a physical model of the plume as a nearly transparent stream of micron-sized alumina particles at their melting points. This spectral shape serves as the reference model spectrum. A comparison of the results for the four UVPI filters indicates that the reference spectral shape is not inaccurate, but the new data suggest a stronger component in the far ultraviolet (UV) ($\lambda < 300$ nm) than the reference model predicts.

The base of UV radiometric data being assembled by the UVPI will be a foundation for further analysis yielding refined interpretations and evaluation. Comparison with models and with data from sensors on other platforms will also yield improved radiometric results and an enhanced phenomenological understanding of UV emission by solid rocket motors in the upper atmosphere.

ULTRAVIOLET PLUME INSTRUMENT DESCRIPTION AND PLUME DATA REDUCTION METHODOLOGY

1.0 INTRODUCTION

This report briefly describes the Ultraviolet Plume Instrument (UVPI) and the methodology being used to reduce the data it gathers on rocket plumes.* The report begins with some background on the UVPI experiment, a brief description of the instrument, and a brief statement of the spectral bands and efficiencies. In addition, the data calibration procedure and some examples of images being processed are presented. This is followed by a substantial presentation of the methods and formulas used in extracting radiometric information. Effects of the point spread function (PSF) and red leakage are discussed. Finally, noise, sensitivity, and error analysis are described.

1.1 Background

The Ultraviolet Plume Instrument is carried aboard the Low-power Atmospheric Compensation Experiment (LACE) spacecraft. The UVPI's mission is to collect images of rocket plumes and to collect background image data of Earth, Earth's limb, and celestial objects in the near and middle ultraviolet wavebands. Five rocket firings were observed. Background object imagery already collected with the UVPI includes the day and night Earth limb air glow, aurora, sunlit and moonlit clouds, solid Earth scenes with varying solar illumination, cities, and stars.

The LACE satellite was designed and built by the Naval Research Laboratory (NRL) in Washington, D.C. The UVPI was assigned to the LACE spacecraft's experiment complement after the spacecraft was designed and its fabrication was begun. Therefore, the UVPI was constrained in size, weight, power consumption, and telemetry to whatever margin remained on the LACE spacecraft.

The requirement that the UVPI be capable of highly accurate pointing from a gravity gradient stabilized spacecraft where the instrument did not have direct access to spacecraft attitude measurements led to a requirement for flexible software to control the instrument.

The satellite (Fig. 1) was launched on 14 February 1990, into a circular orbit at an altitude of 292 nautical miles and a 43° inclination. The spacecraft weighs 3175 lb. The body of the spacecraft is box shaped, 4.5 by 4.5 ft and 8 ft high. Gravity gradient stabilization is provided by a 150-ft retractable boom with a 200 lb mass emerging from the top of the spacecraft. The LACE spacecraft was designed to support its experiment complement for 30 months and has no orbit adjustment capability.

NRL operates three ground stations to communicate with and control the satellite. Typical UVPI observations range from 3 to 10 minutes and usually include between 2,000 and 5,000 images. Data are channeled to the UVPI Mission Planning and Assessment Center in Alexandria, Virginia, for processing and evaluation. More than 200 observations were logged in 2 years of operation. Data tapes are archived in the SDIO Background Data Center at NRL for further distribution.

---

* For your convenience, a Glossary is placed at the end of this report.

Manuscript approved October 1, 1992.

1.2 UVPI Brief Description

The UVPI sensor assembly [1-2] contains two coaligned camera systems that are used in concert to acquire the object of interest, control UVPI, and acquire UVPI images and radiometric data. The two camera systems are the tracker camera and the plume camera; these are discussed briefly below. The two cameras share a fixed 10-cm diameter Cassegrain telescope that uses a gimbaled plane steering mirror to view a field of regard that is a 50° half-angle cone around the nadir. In addition, UVPI contains a second plane mirror on the instrument door. This mirror can be set at an angle of approximately 45° relative to the nadir and used in conjunction with the steering mirror to view the Earth limb and stars near the limb. Appendix A describes the configuration of the UVPI in detail; Section 2.0 discusses the radiometric response of UVPI. The characteristics of the UVPI have been previously reported [2-3].

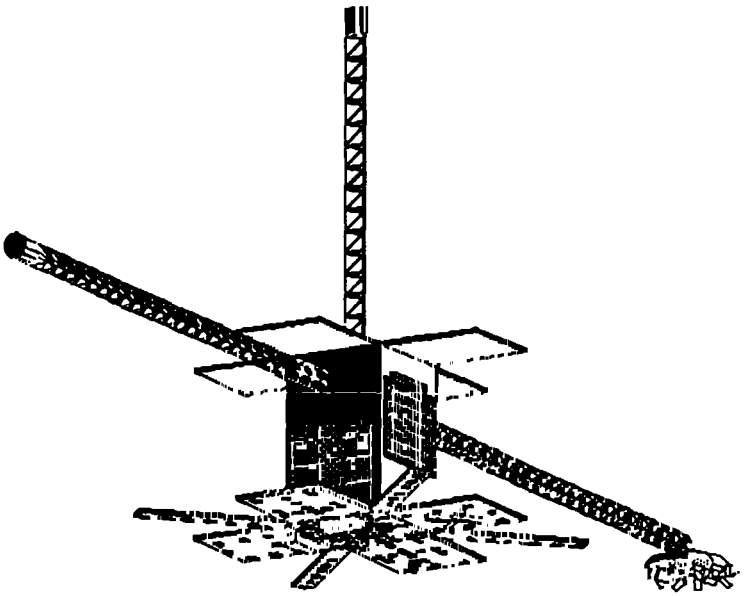

Fig. 1 - Schematic of LACE satellite

The tracker camera has a relatively wide total field of view of 1.98° by 2.60°; images over this full field of view can be recorded at a 5 Hz image rate. The tracker camera can also be operated in a mode where the transmitted field of view is restricted to the central 17% of the full field of view, and the image rate is increased to 30 Hz. The intensifier gain and the exposure time of the camera can be controlled to provide a radiometric dynamic range greater than 10^6.

The tracker camera has three primary functions that are important for UVPI operation. First, the tracker camera, with its wide field of view and bright image, is used to acquire the object or image of interest. Second, the tracker camera image can be processed on board UVPI if desired, and the result can be used to control the gimbaled mirror so that UVPI autonomously tracks the object of interest. Third, the tracker camera is calibrated so that it can acquire radiometric data within its bandpass.

The plume camera is also an intensified charge-coupled device (CCD) camera operating in the ultraviolet. The plume-camera optical train contains a filter wheel with four selectable filters having bandpasses in the 195 to 350-nm range . The plume camera has a total field of view of 0.184° by 0.137° and has a correspondingly higher resolution than can be achieved by the tracker camera. Images over the full plume-camera field of view can be recorded at a 5 Hz image rate. Like the tracker camera, the plume camera can also be operated in a mode where the field of view is restricted

to the central 17% of the full field of view, and the image rate is increased to 30 Hz. The intensifier gain can be controlled to provide a radiometric dynamic range greater than 10^6.

The primary function of the plume camera is to acquire images and radiometric data within the four selectable wavelength bands. UVPI was not designed to use the plume camera for tracking because of the relatively dim images expected in these wavelength bands.

In typical operation, the UVPI is programmed via ground command to point the gimbaled mirror at the expected location of the plume or other object of interest. UVPI then enters a selected scan pattern until the desired object enters the field of view of the tracker camera. The tracker camera and control electronics on board UVPI then track the object, and both cameras gather image and radiometric data. The plume camera filter can be changed as desired during the data collection to select wavelength bandpasses. If the plume or object of interest is temporarily lost as a result of a coasting phase between rocket stages or some other reason, UVPI can be commanded to enter various extrapolation or search modes as required. Table 1 provides a brief summary of the instrument characteristics.

Table 1 - Instrument Characteristics

Parameter	Tracker Camera	Plume Camera
Shared telescope type	Maksutov Cassegrain	Maksutov Cassegrain
Telescope diameter	10 cm	10 cm
Focal length	60 cm	600 cm
Field of view	2.60° x 1.98°	.184° x .137°
Field of regard	100° x 97°	100° x 97°
Field of view per pixel	180.5 x 143.9 μrad	12.8 x 10.0 μrad
Pixel footprint @ 500 km	90 x 72 m	6.4 x 5.0 m
System resolution (FWHM)	220 to 250 μrad	80 to 100 μrad
Spectral region	255 - 450 nm	195 - 350 nm
Number of filters	1	4
Photocathode material	Bialkali	CsTe
Time for filter change	n/a	1.7 s
Digitization	8 bits/pixel	8 bits/pixel
Digital data rate	2.5 Mbps	2.5 Mbps
Image rate: Normal	5 per s	5 per s
Zoom*	30 per s	30 per s
Pixels: Normal	251 x 240	251 x 240
Zoom	91 x 112	91 x 112
Pixel exposure time	.16 to 33.3 ms	33 ms
Frames integrated	n/a	1 - 6
Exposure range	$>10^6$	$>10^6$
Noise-equivalent radiance	See Section 7.2 for detailed discussion. NER depends on gain setting and filter selected.	

*Reduced field of view.

1.3 UVPI Spectral Response

The UVPI plume and tracker cameras are described in detail in Appendix A. The optical paths for both the plume and tracker camera systems can be divided into two parts. The first part of each consists of the telescope, a bandpass filter to select the observation wavelength, and the photocathode of the image intensifier. For the plume camera, one of four bandpass filters can be

selected and the photocathode material is CsTe. For the tracker camera, only one bandpass filter is available and the photocathode material is bialkali.

The second part of each camera system consists of the remaining elements of the image intensifier: the fiber-optic reducer, the CCD, and the electronics, which convert the pixel response to a digital number. The gain of each image intensifier is selectable, and the exposure time of the tracker camera is selectable by strobing the intensifier high voltage. The response of the UVPI cameras can be divided into the gains of the two parts described above.

The first component of the response for each camera is the net quantum efficiency, which is the probability that a photon incident on the UVPI telescope will produce a photoevent (PE). A photoevent is defined as a photoelectron at the photocathode that is collected and amplified by the microchannel plate (MCP). This component of the response is wavelength-dependent. It corresponds primarily to the filter bandpasses but also includes the wavelength dependence of the optics and photocathodes. The collection efficiency of the MCP is incorporated into this component.

The second component of the response for each camera is the conversion ratio between photoevents and the digital number reported by the CCD control electronics. It is this digital number that is reported for each pixel in the telemetry stream. This component is not wavelength-dependent and takes into account MCP gain, phosphor, and CCD efficiencies.

The net quantum efficiency for the plume and tracker cameras are discussed in this section. The conversion of photoevents per pixel to a digital number in telemetry is discussed in the next section.

The response of the UVPI plume and tracker cameras as a function of wavelength in the ultraviolet was carefully measured before launch. Figure 2 shows the net quantum efficiency of the plume camera for each of the four bandpass filters. Table 2 shows the bandpass limits λ_1 and λ_2 chosen for each filter. The net quantum efficiency of the tracker camera is shown in Fig. 3. The values of net quantum efficiency plotted in these figures are given in Tables 3 and 4.

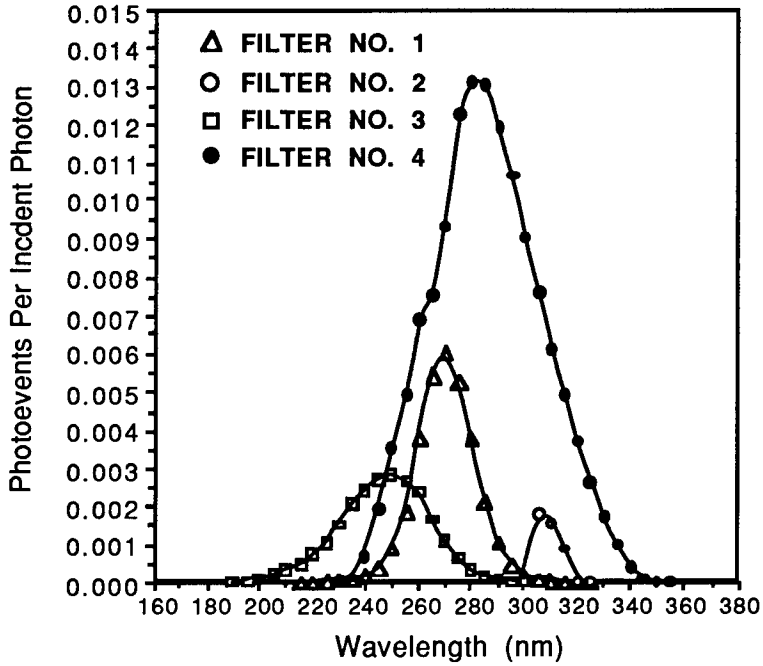

Fig. 2 - Plume camera - net quantum efficiency curves

Table 2 - Bandpasses

Camera/ Filter	λ_1 (nm)	λ_2 (nm)	λ_2-λ_1 (nm)	FWHM (nm)
Plume PC-1	220	320	100	25
Plume PC-2	300	320	20	10
Plume PC-3	195	295	100	50
Plume PC-4	235	350	115	56
Tracker	255	450	195	150

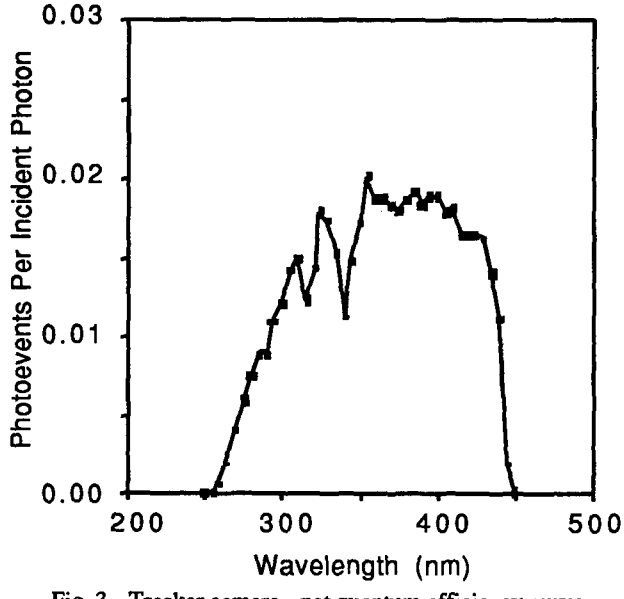

Fig. 3 - Tracker camera - net quantum efficiency curve

1.4 Overview of UVPI Data Reduction Methodology

UVPI collects rocket plume data in the form of digitized images. The method used in the reduction of UVPI images implies a stochastic system model in which the continuous spatial, temporal, and spectral rocket plume signal is sampled and converted to discrete values or digital numbers (DN).

Subsection 1.4.1 describes such a system-level model of UVPI. This is followed in Subsection 1.4.2 by an overview of the data reduction process used to work backwards to derive the implied radiance of the source.

1.4.1 *Equivalent UVPI Imaging System Model*

Figure 4 is a simplified block diagram of the signal path in the UVPI imaging system. This type of diagram illustrates how the inherent rocket plume and background signal information is modified as it passes through the imaging system. Signal degradation shows up in the measured image as point spread function effects followed by all other noise effects. In this diagram the signal flows from left to right. This model is an equivalent imaging model since similar sources of image degradation, such as spatial blurring of the signal, are lumped together at one point in the model. A brief description of this diagram is in order.

Table 3 - Net Quantum Efficiency for Plume Camera

Wavelength (nm)	PC-1 (PE/photon)	PC-2 (PE/photon)	PC-3 (PE/photon)	PC-4 (PE/photon)
195	–	–	6.06×10^{-5}	–
200	–	–	1.29×10^{-4}	–
205	–	–	2.18×10^{-4}	–
210	–	–	3.27×10^{-4}	–
215	–	–	4.64×10^{-4}	–
220	1.38×10^{-5}	–	7.09×10^{-4}	–
225	3.76×10^{-5}	–	1.07×10^{-3}	–
230	7.38×10^{-5}	–	1.55×10^{-3}	–
235	9.17×10^{-5}	–	2.09×10^{-3}	1.18×10^{-4}
240	2.00×10^{-4}	–	2.47×10^{-3}	6.77×10^{-4}
245	3.84×10^{-4}	–	2.73×10^{-3}	1.98×10^{-3}
250	8.81×10^{-4}	–	2.84×10^{-3}	3.52×10^{-3}
255	1.87×10^{-3}	–	2.70×10^{-3}	4.93×10^{-3}
260	3.80×10^{-3}	–	2.42×10^{-3}	6.92×10^{-3}
265	5.46×10^{-3}	–	1.68×10^{-3}	7.54×10^{-3}
270	6.06×10^{-3}	–	1.12×10^{-3}	9.32×10^{-3}
275	5.30×10^{-3}	–	6.38×10^{-4}	1.23×10^{-2}
280	3.81×10^{-3}	–	3.44×10^{-4}	1.31×10^{-2}
285	2.11×10^{-3}	–	1.83×10^{-4}	1.31×10^{-2}
290	1.03×10^{-3}	–	1.24×10^{-4}	1.19×10^{-2}
295	4.81×10^{-4}	–	5.19×10^{-5}	1.07×10^{-2}
300	2.07×10^{-4}	5.37×10^{-5}	1.70×10^{-5}	9.05×10^{-3}
305	9.39×10^{-5}	1.82×10^{-3}	7.00×10^{-6}	7.64×10^{-3}
310	5.34×10^{-5}	1.60×10^{-3}	4.93×10^{-6}	6.13×10^{-3}
315	1.58×10^{-5}	9.06×10^{-4}	3.24×10^{-6}	4.96×10^{-3}
320	3.95×10^{-6}	2.05×10^{-5}	1.95×10^{-6}	3.77×10^{-3}
325	2.55×10^{-6}	1.15×10^{-6}	1.05×10^{-6}	2.66×10^{-3}
330	1.49×10^{-6}	1.94×10^{-7}	4.60×10^{-7}	1.74×10^{-3}
335	7.36×10^{-7}	1.03×10^{-7}	2.32×10^{-7}	9.84×10^{-4}
340	2.48×10^{-7}	1.29×10^{-8}	8.14×10^{-8}	4.12×10^{-4}
345	1.22×10^{-7}	6.76×10^{-9}	4.02×10^{-8}	1.18×10^{-4}
350	3.57×10^{-8}	6.19×10^{-10}	1.27×10^{-8}	4.60×10^{-6}
355	1.94×10^{-8}	5.15×10^{-10}	6.63×10^{-9}	8.32×10^{-7}
360	1.42×10^{-8}	4.11×10^{-10}	5.19×10^{-9}	2.04×10^{-7}

For the case of rocket plume observations, there are two additive sources of average spectral irradiance at the entrance of the UVPI sensor pupil. The first source is the spectral irradiance coming from the object under observation, i.e., the rocket plume. The second source is the spectral irradiance not related to the object under observation, e.g., background clutter. In this report the desired signal is considered to be the rocket plume signal itself. Immediately after passing through the sensor pupil, the combined spectral signal flows into the spectral filter block. At this point the signal is folded with the active UVPI spectral filter and integrated in time. The spectral folding equates to performing a weighted spectral integral of the signal with the net quantum efficiency of the active filter. This is discussed in Section 1.3.

Table 4 - Net Quantum Efficiency for Tracker Camera

Wavelength (nm)	Tracker NQE	Wavelength (nm)	Tracker NQE
255	1.09×10^{-5}	355	2.00×10^{-2}
260	5.86×10^{-4}	360	1.87×10^{-2}
265	1.81×10^{-3}	365	1.87×10^{-2}
270	3.98×10^{-3}	370	1.82×10^{-2}
275	5.88×10^{-3}	375	1.80×10^{-2}
280	7.30×10^{-3}	380	1.86×10^{-2}
285	8.86×10^{-3}	385	1.91×10^{-2}
290	8.90×10^{-3}	390	1.80×10^{-2}
295	1.09×10^{-2}	395	1.86×10^{-2}
300	1.21×10^{-2}	400	1.86×10^{-2}
305	1.40×10^{-2}	405	1.79×10^{-2}
310	1.50×10^{-2}	410	1.81×10^{-2}
315	1.23×10^{-2}	415	1.64×10^{-2}
320	1.43×10^{-2}	420	1.64×10^{-2}
325	1.79×10^{-2}	425	1.64×10^{-2}
330	1.74×10^{-2}	430	1.61×10^{-2}
335	1.52×10^{-2}	435	1.39×10^{-2}
340	1.12×10^{-2}	440	1.10×10^{-2}
345	1.47×10^{-2}	445	1.79×10^{-3}
350	1.71×10^{-2}	450	8.75×10^{-5}

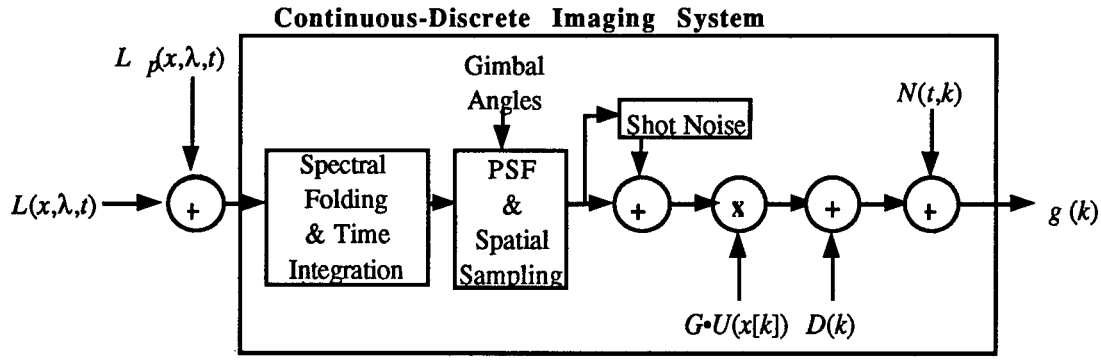

Legend:
- $L(x,\lambda,t)$ - Spectral irradiance at sensor pupil coming from object under observation
- $L_p(x,\lambda,t)$ - Spectral irradiance at sensor pupil not related to object under observation
- G - Conversion constant, photoevents (PE) per digital number (DN)
- $U(x[k])$ - Detector nonuniformity at the kth pixel location
- $D(k)$ - Dark field at the kth pixel location
- $N(t,k)$ - Temporal noise sources (zero mean), e.g. thermal, quantization (A/D)
- $g(k)$ - Discrete output image in digital numbers (DN) at pixel location k

Fig. 4 - Simplified block diagram of signal path in the UVPI

Following the signal flow shown in Fig. 4, at the next stage the signal is convolved with the equivalent system-level point spread function (PSF) and spatially sampled over a rectangular lattice. The UVPI point spread function is defined as the response of the UVPI cameras to a point source, e.g., a star or a ground beacon. It effectively changes the spatial frequency content of the image from that of the original signal, e.g., blurring of the observed data occurs, resulting in a loss of image fidelity. The PSF is closely related to the system modulation transfer function (MTF). For UVPI, the spatial degradations are primarily introduced by diffraction-limited properties of optical elements, bandwidth limitations and transients in the electronic components, sensor jitter, and gimbal angle changes within the focal plane array integration time. Section 5.0 provides quantitative information related to the UVPI PSF. Based on in flight analysis, it is reasonable to model the UVPI PSF as a space invariant function.

Other signal degradations affect only individual image points (pixels). These include shot noise, quantization noise, and thermal noise.

Shot noise is an additive noise that is signal level dependent. In this equivalent model, the output of this stage, after the shot noise is added, results in a signal with a Poisson distribution having a mean equal to the mean number of photoevents observed and a standard deviation proportional to the square root of the mean of photoevents observed. Section 7.1 presents the empirically derived relation for the standard deviation.

The next two stages in the equivalent model characterize the focal plane array response under the assumption of no detector noise. The output of each pixel in the focal plane array can be modeled, within the dynamic range of the detector, as a linear response with a nonzero intercept as a function of signal level. Since not all the pixels in the FPA have exactly the same linear response, two matrices are used to characterize the FPA. The first matrix is the detector nonuniformity matrix U, which characterizes the response or slope associated with each pixel. The second matrix is the FPA dark field matrix D. This is equivalent to the response of each pixel when no input signal is present, i.e., the zero intercept. For any given observation, both of these matrices are considered to be fixed or deterministic in nature. Sections 2.1 and 2.2 provide, respectively, quantitative information on the nonuniformity and dark field matrices. The constant G accounts for the conversion from photoevents to digital numbers at the gain of the cameras.

Finally, a more realistic detector model is achieved by adding the thermal and quantization noise terms to the resulting signal on a pixel by pixel basis. These two noise sources are signal-level independent. Quantization noise is an equivalent noise introduced in the analog-to-digital (A/D) conversion process. It is normally modeled by a uniform distribution with zero mean and standard deviation of 1/12. Thermal noise is modeled by a gaussian distribution with zero mean and a standard deviation that is temperature dependent. In actual practice, thermal and quantization noise are observed simultaneously. Therefore, empirical estimates of the combined noise sources can be obtained during dark field estimates.

In summary, the output of the image formation process corresponds to measurements of the image intensity over a lattice grid. Unfortunately, because of the inherent spatial and point degradations in the system, the output of this process is more accurately modeled as the sampled output of a linear system plus additive noise. The next section discusses the steps taken to remove all the deterministic transformations to which the original irradiance signal is subjected.

1.4.2 *Simplified UVPI Data Reduction Model*

Figure 5 is a block diagram showing the basic sequence of data reduction steps used to recover the original source radiance. There are two major blocks in these diagrams: nominal data reduction, which primarily involves the calibration of each UVPI image; and additional data reduction, which usually involves some special analytic processing. A brief description of this diagram and the processes is given.

For nominal data reduction the digital numbers received from the satellite, in the form of 8 bits/pixel, are converted to counts of photoevents/s/pixel. In this process, all the nonrandom

transformations introduced into the original signal are removed except the blurring introduced by the PSF.

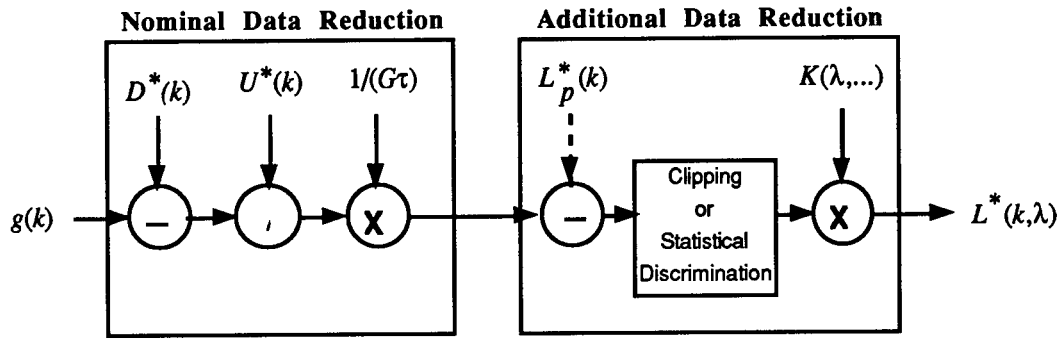

Legend:
- $g(k)$ - Measured discrete image value in digital numbr at pixel location k
- $U^*(k)$ - Estimated detector nonuniformities at pixel location k
- $D^*(k)$ - Estimated dark field at pixel location k
- $P^*(k)$ - Estimated number of photoevents at pixel location k
- $L^*_p(k)$ - Estimated in-band path radiance (PE/s-pixel)
- $K(\lambda,...)$ - Radiometric conversion function at pixel location k
- $1/(G\tau)$ - Conversion to photoevents(PE)/s
- $L^*(k,\lambda)$ - Estimated target spectral radiance with no corrections for PSF effects

Fig. 5 - Simplified UVPI data reduction block diagram

The first stage in the data reduction process is to subtract an estimate of the deterministic dark field matrix. If the signal level is low at any given pixel, it is possible that a negative number results after performing the dark field subtraction for that pixel. This is primarily due, as discussed in the previous section, to the presence of additive noise in the signal. Section 2.1 discusses the procedure used to estimate the dark field matrices.

The second data reduction stage is to normalize every pixel by the estimate of the nonuniformity matrix. Section 2.2 discusses the procedure used to estimate the nonuniformity matrix.

The estimation of both the dark field matrix and the nonuniformity matrix are critical for obtaining accurate, unbiased estimates of the signal. If the estimate of the dark field matrix is in error by a constant value, a bias will be obtained on every pixel.

The normalization of the data by the gain conversion factor G_g converts the resulting image to units of photoevents/s/pixel. Section 2.4 discusses how G_g was estimated and validated by using in flight calibration star observations.

For rocket plume observations, additional data reduction is performed to obtain accurate radiometric numbers. The first stage in the additional data reduction process is to remove any left-over bias that is detected in regions where it is known that no signal should be present. If detected, the bias level is estimated and removed from every pixel in the image. If no superposition of frames is to be performed, the next stage is to perform an optional clipping of the data to suppress any readout of negative number of photoevents/s/pixel. Finally, given a reference spectrum, an estimate of the spectral irradiance can be obtained. Section 4.0 provides an in-depth description of how this process is done for UVPI.

By registering, if necessary, and then summing consecutive images resulting from this processing stage, an increase in signal-to-noise ratio (SNR)/pixel can be achieved. Section 7.2 discusses how the sensitivity of UVPI is increased by image processing the data. No attempt is being made at the present time to remove any of the spatial blurring introduced by the UVPI PSF from the measured images.

2.0 DATA CALIBRATION PROCEDURE

The raw image data transmitted from the satellite is in the form of arrays of 8-bit binary numbers Q_k, which represent the intensity of light falling on the kth pixel of the CCD. These Q_k are converted into the number of photoevents P_k occurring at the corresponding photocathode location during the image frame:

$$P_k = (1/G_g)[Q_k - D_k]/U_k,$$

where

G_g is gain conversion factor for gain step g, i.e., the value of Q_k for a single photoevent, assumed to be the same for all pixels k;
D_k is the dark value for the kth pixel; and
U_k is the gain nonuniformity correction factor for the kth pixel.

The pulse height distribution of the image intensifier will cause noninteger values for P_k. The conversion of CCD response peaks to integral photoevent counts is possible only on the weakest images because of the overlap of photoevent images. Hence, P_k values are treated as continuous variables. The G_g, D_k, and U_k factors are summarized in the following paragraphs.

2.1 Dark Field D_k

Dark field images are collected with the UVPI door closed. The pixel brightness results from two sources: dark current in the photocathode, microchannel plate, and charge-coupled device; and a fixed bias voltage on the readout line. The dark current component has fixed-pattern spatial variations that can be accurately determined by averaging a large number of frames. The bias voltage component contributes some spatially and temporally random noise.

The dark field average used for calibration is usually generated from data collected during the same observation pass. Analysis shows that, as expected, average dark field values do not depend significantly on microchannel plate gain step. However at high gain steps, occasional responses resulting from cosmic rays or thermally generated electrons from the photocathode are evident.

Typically, for the tracker camera the spatial mean of the temporal mean pixel values is in the range 19 to 20 digital numbers (DN), and the spatial mean of the temporal standard deviation in pixel values is in the range 1 to 2 DN. For the plume camera, the spatial mean of the temporal mean pixel values is in the range 9 to 10 DN, and the spatial mean of the temporal standard deviation in pixel values is approximately 1 DN. To obtain a good estimate of the dark field mean value, the average number of frames used is typically 100. Where the standard deviations of the cameras are expressed in DN, the values are independent of gain; but if they are expressed in photoevents, they vary with gain step. See Table 5.

For gain levels 7 through 15 of the plume camera, which cover almost any rocket observation, the noise in the dark field is less than 1 photoevent per image on the average. For the tracker camera the noise is higher, but the signals tend to be much higher also. For the lower gain levels, the dark field noise can be a significant contributor.

2.2 Spatial Nonuniformity U_k

Tracker and plume camera nonuniformity matrices are typically generated by using several images that look down at the ocean. For the tracker camera, the images of small moving clouds can be removed by selecting the minimum value in a temporal sequence of images on a pixel-by-pixel basis. The scene is sufficiently bright that photon shot noise is a negligible percentage of the mean value. For the plume camera, sequences of images taken with filter 4 are averaged. Since the plume camera's field of view is relatively narrow, it is easily possible to average sequences of frames that are free of clouds.

For the central 91 by 112 pixels transmitted using the high image transmission rate, overall nonuniformity is less than 4%. A histogram is shown in Fig. 6. The error caused by uncertainty in the factor U_k is less than 1%.

Although some spatial nonuniformities in the phosphor, MCP, photocathode, and CCD have been found to remain constant at all times, it is evident that certain blemishes visible in plume camera flatfield images are filter-position-dependent. Clearly, these blemishes are in the spectral filters themselves because they move with the filter wheel as it rotates between filter positions. Furthermore, after the filter wheel has moved, either during a single pass or between passes, a return to a particular filter position shows slight changes in the appearance of the blemishes, i.e., the blemish sizes and positions are not perfectly repeatable.

The filter blemishes appear in flatfield images as dark spots, probably shadows, that shift and spread or contract slightly each time the filter wheel is rotated. This shifting and spreading indicates that the filter wheel may be slightly loose in the plane normal to the optical axis. The result is that correction for these blemishes can be very difficult. Near flatfield observations such as daytime nadir viewing over the ocean, land, or uniform clouds can, with some effort, be corrected on a frame-by-frame basis. Less uniform sources, which do not show the filter blemishes clearly, may not be correctable. Table 6 lists the approximate pixel locations of the blemishes. In general, the effect of the blemishes is localized and probably relatively insignificant.

Table 5 - Dark Field Noise (Photoevents/Pixel-Image)

Gain Step	Plume Camera Dark Field Noise (Photoevents)	Tracker Camera Dark Field Noise (Photoevents)
0	$4.62 \times 10^{+1}$	$1.18 \times 10^{+3}$
1	$3.36 \times 10^{+1}$	$6.16 \times 10^{+2}$
2	$1.85 \times 10^{+1}$	$2.85 \times 10^{+2}$
3	$1.19 \times 10^{+1}$	$1.35 \times 10^{+2}$
4	7.39	$6.47 \times 10^{+1}$
5	3.40	$2.85 \times 10^{+1}$
6	1.31	$1.48 \times 10^{+1}$
7	5.53×10^{-1}	8.10
8	2.47×10^{-1}	3.73
9	1.17×10^{-1}	1.91
10	5.45×10^{-2}	9.87×10^{-1}
11	3.43×10^{-2}	4.65×10^{-1}
12	1.76×10^{-2}	2.34×10^{-1}
13	9.61×10^{-3}	1.02×10^{-1}
14	8.21×10^{-3}	6.68×10^{-2}
15	8.21×10^{-3}	4.19×10^{-2}

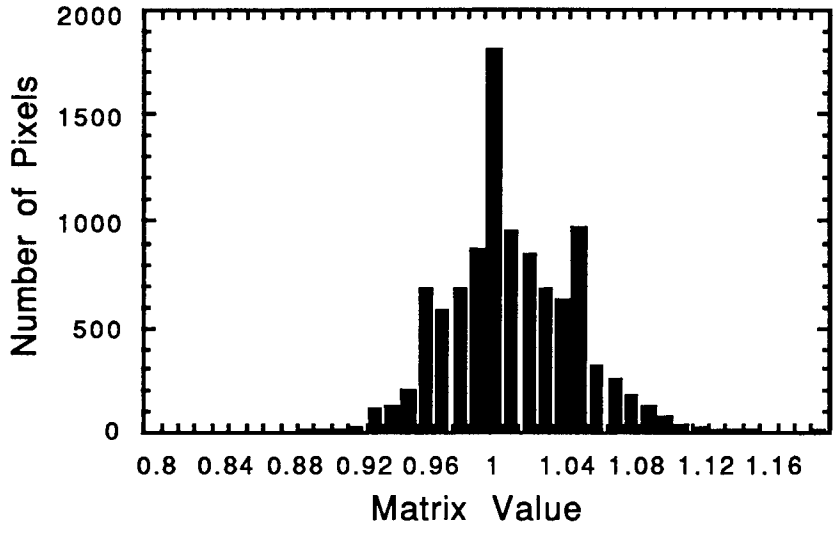

Fig. 6 - Inverse nonuniformity matrix histogram

Table 6 - Location and Size of Filter Blemishes

Spectral Filter	Blemish Number	Location of Center Pixel (Row, Column)	Size (pixels)
1	1	(38,204)	6 pixel radius
2	1	(134,214)	4 pixel radius
3	none		
4	1	(87,13)	4 x 5
4	2	(101,29)	5 x 3
4	3	(67,37)	5 x 4
4	4	(79,49)	3 x 3
4	5	(157,103)	3 x 3
4	6	(125,113)	8 x 4
4	7	(103,113)	4 x 2
4	8	(147,175)	4 x 3
4	9	(153,213)	5 x 3
4	10	(157,237)	4 x 3

The tracker camera shows only minor nonuniformities, and none appear to be associated with the spectral filter.

The nonuniformity matrix used for calibration of UVPI plume camera data is filter-blemish-independent. Because of the unpredictable nature of the blemishes, no attempt is made to correct for them.

2.3 Gain Conversion Factor G_g

It is assumed that the net quantum efficiency curves shown in Figs. 2 and 3 remain constant under all measurement conditions. Therefore, variations in the responsivity of the instrument are taken into account in the gain conversion factor G_g for the gth gain step. The values of G_g are not dependent on wavelength but are dependent primarily on microchannel plate gain step. They also reflect the phosphor and CCD efficiencies, which appear to be fairly constant in time. To a lesser extent, the G_g values depend on sensor temperature and, possibly, pass-specific parameters. The values of G_g are given for the tracker camera in Table 7, and for the plume camera in Table 8. The units for G_g are digital number per photoevent.

Table 7 - Gain Conversion Factor G_g for Tracker Camera

Gain Step g	Gain Conversion Factor G_g (digital number per photoevent)
15	120.8
14	45.6
13	25.4
12	10.15
11	4.88
10	2.30
9	1.19
8	0.612
7	0.280
6	0.149
5	0.0797
4	0.0348
3	0.0166
2	0.00791
1	0.00366
0	0.00190

The values of G_g for all gain steps were measured before launch. In addition, the value for gain step 15 was determined by using sparse-field data for which single isolated photoevents are generated from dark-noise or low-level illumination. The values for all pixels associated with each isolated photoevent are summed; the resulting sum is the G_g value for this step. Finally, on-orbit calibrations for all plume- and tracker-camera bandpasses were performed. These are discussed in the next section. The on-orbit calibrations are used as the primary instrument calibration. These calibrations remained constant throughout the first two years of operation.

2.4 On-Orbit Confirmation of Gain Conversion Factor

The radiometric calibration constants for the UVPI were confirmed on orbit. This was done by measuring the sensor output for a star and comparing it with the predicted number of photoevents based on the star's spectrum and brightness. The ratio of these two quantities is the gain conversion factor G_g for the gain step used in the measurement. The process is repeated using several stars at a variety of UVPI gain steps. The predictions of the number of photoevents from a star are based on measured stellar emission spectra obtained by the International Ultraviolet Explorer (IUE) and

Orbiting Astrophysical Observatory (OAO) satellites [4,5]. Spectral information spanning the Balmer discontinuity and extending to longer wavelengths was obtained from atmosphere-corrected ground-based measurements [6]. Absolute errors associated with these measured spectra are probably less than 10%, but probably are significant contributors to the scatter in star calibration data points. Also, some scattered light reaching the focal plane contributes significantly to the variation, especially for the tracker camera. The measured scatter, reported as average deviation from the mean calibration curve, is included in Table 9.

Table 8 - Gain Conversion Factor G_g for Plume Camera

Gain Step g	Gain Conversion Factor G_g (digital number per photoevent)
15	293
14	221
13	144
12	77.6
11	39.8
10	23.2
9	10.81
8	5.13
7	2.29
6	0.951
5	0.378
4	0.169
3	0.105
2	0.0675
1	0.0371
0	0.0270

Table 9 - Error in $1/G_g$ for Tracker and Plume Cameras

Camera/Filter	Average Deviation from Calibration Curve (%)	Maximum Deviation from Calibration Curve
Tracker	15.6	17.3
Plume, PC-1	10.5	33.3
Plume, PC-2	15.9	25.2
Plume, PC-3	9.9	24.7
Plume, PC-4	13.5	26.0

Figures 7 and 8 show calibration results for the plume camera and tracker camera, respectively. Figure 7 shows calibration points for all four plume camera filters. The solid curve shown in each figure is very close to that measured before launch; these star measurements are the primary calibration for the UVPI. The stars used for calibration were mostly type B stars of sufficiently high temperatures that they were strong emitters in the ultraviolet and made any long-

wavelength response of the UVPI insignificant. The on-orbit calibration measurements indicate that the UVPI responsivity had remained constant since launch.

Table 9 tabulates the error associated with the gain conversion factor for the plume and tracker cameras. The average deviation is a good error estimate; the maximum deviation gives worst case estimate.

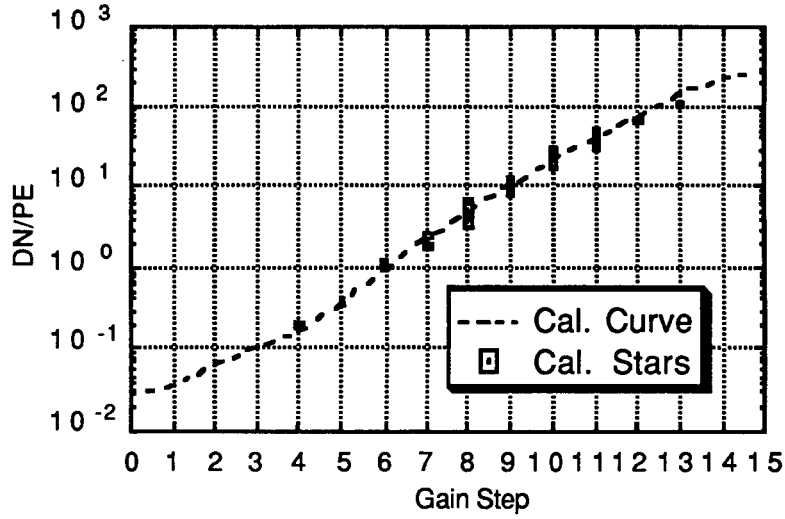

Fig. 7 - Star measurements for plume camera

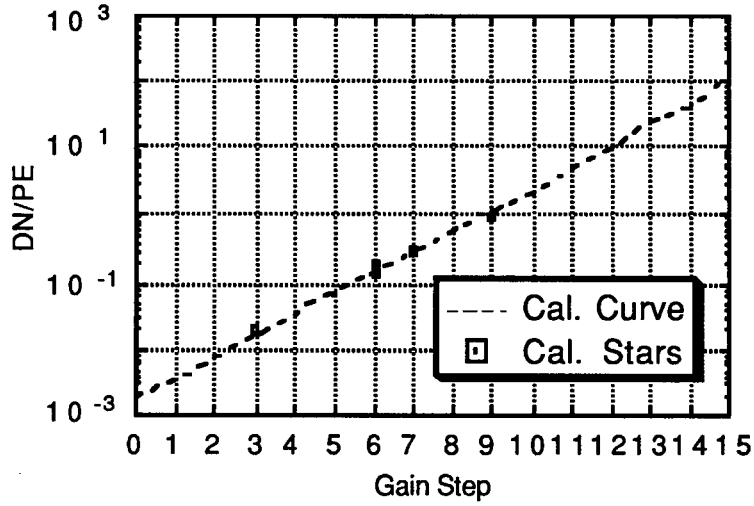

Fig. 8 - Star measurements for tracker camera

3.0 EXAMPLES OF PROCESSED IMAGES

3.1 Single Images Before and After Calibration

This subsection presents four single uncalibrated plume images and one calibrated plume image. Given the characteristics of the UVPI cameras, e.g., exposure time, optics aperture, and rocket plume radiant intensity, the number of photoevents that are registered within the focal plane array of a camera can be individually counted as isolated events. In this respect, UVPI can be used as a photon-counting instrument.

Figure 9 shows samples of single images, in high image transmission rate, of the Antares rocket burn for the plume-camera filters. The image in the upper left corner is for PC-4; the upper right corner is for PC-3; the lower left corner is for PC-2; and the lower right corner is for PC-1. Pixel radiance is encoded as image brightness, where dark and bright are, respectively, relatively smaller and larger radiance. The images demonstrate that the shape of the plume is not necessarily clearly delineated in a single frame. Every bright spot on the image corresponds to one or more photoevents that occur at that particular pixel during the exposure time of the camera.

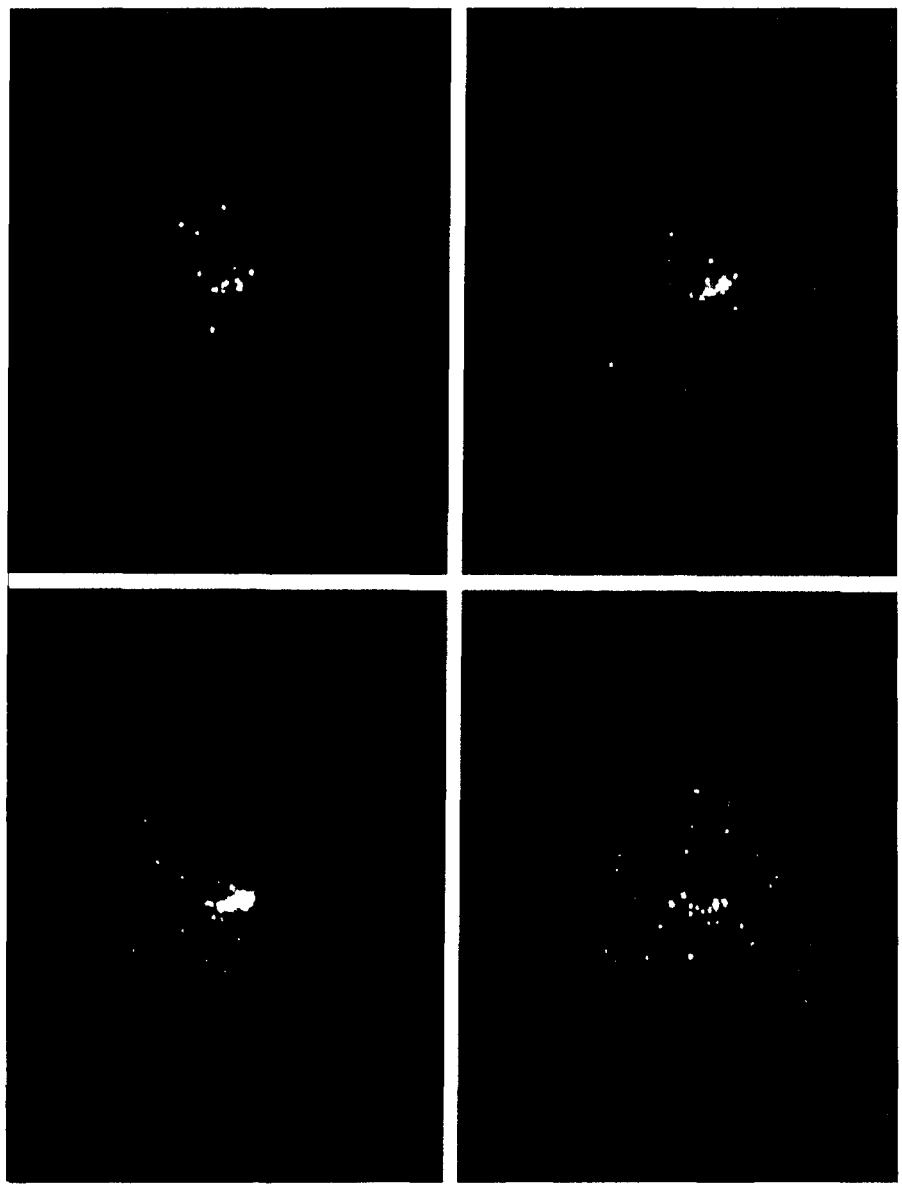

Fig. 9 - Single unprocessed plume-camera images of Antares plume

Figure 10 is a calibrated image illustrating the number of photoevents per second measured at each pixel location in the center 64 by 64 pixels of the lower-left-corner image shown in Fig. 9. The z axis corresponds to the number of photoevents per second; the x and y axes correspond to row and column indices. The actual procedure used to compute the number of photoevents from the measured digital number in the UVPI telemetry stream is discussed in Section 2.0.

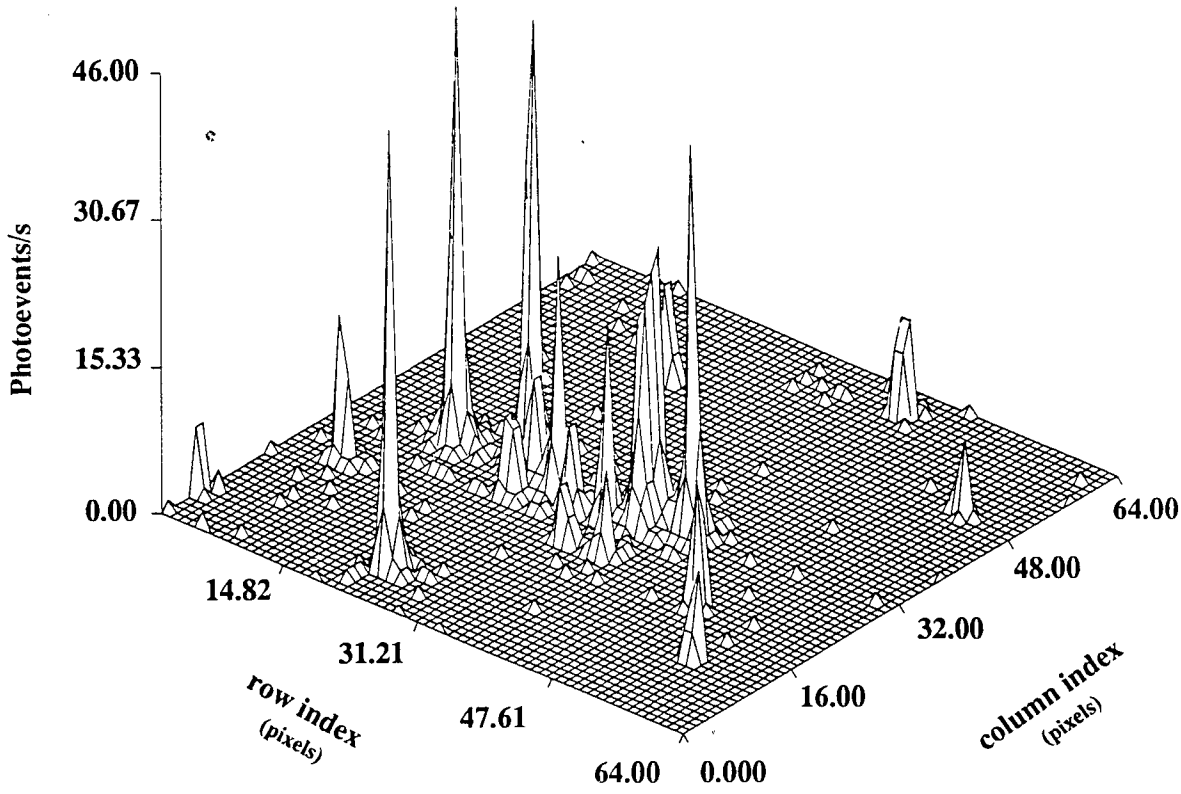

Fig. 10 - Single calibrated plume-camera image of Antares plume

3.2 Composite Images

Figure 11 shows the calibrated composite image obtained by adding single plume-camera images acquired while observing the Antares rocket plume with filter PC-3. The composite image is a result of adding 207 individual calibrated images. The radiant intensity has been mapped to a false-color scale, with black representing the highest intensity, yellow the middle intensity, and white the lowest intensity. A horizontal color bar depicting the mapping of radiant intensity into colors is shown on the lower left corner. A histogram of the image intensity values is shown above the color bar in the form of black dots.

Within this time interval of this composite image, the plume-to-tracker image ratio was 8 to 2, and the exposure time for each individual image was $^1/_{30}$th of a second. Frequently, 100 or more individual images can be superposed to form a composite image of significantly improved SNR. The limit on the number of images that can be added usually depends on smearing caused by the rotation of the images as the satellite passes over the target. A 10° rotation may occur in as little as a few

seconds, so smearing can appear when adding 50 to 100 images collected at the high image transmission rate. See the next section for a discussion of smearing.

3.3 Registration of Images

Typically, composite images are formed by adding values for corresponding pixels over all the images in a data interval. This is done to improve the SNR in each pixel. However, it usually leads to some degree of smearing. The smearing results from pointing jitter and rotation and some distortion of the image because of the changing viewing angle.

The effect of superposing the plume camera images without frame registration can be assessed by computing the average centroid position and the standard deviation of the centroid position over all the images superposed. Table 10 summarizes the centroid position for the plume camera for several composite images of the Antares rocket. The intensity centroid for each image was computed after setting to zero all those pixels with amplitude below 5% of the peak pixel amplitude. It can be seen that maximum RMS jitter was 7.1 pixels. Although this is not negligible, the large effort required for image registration has not been considered to be justified.

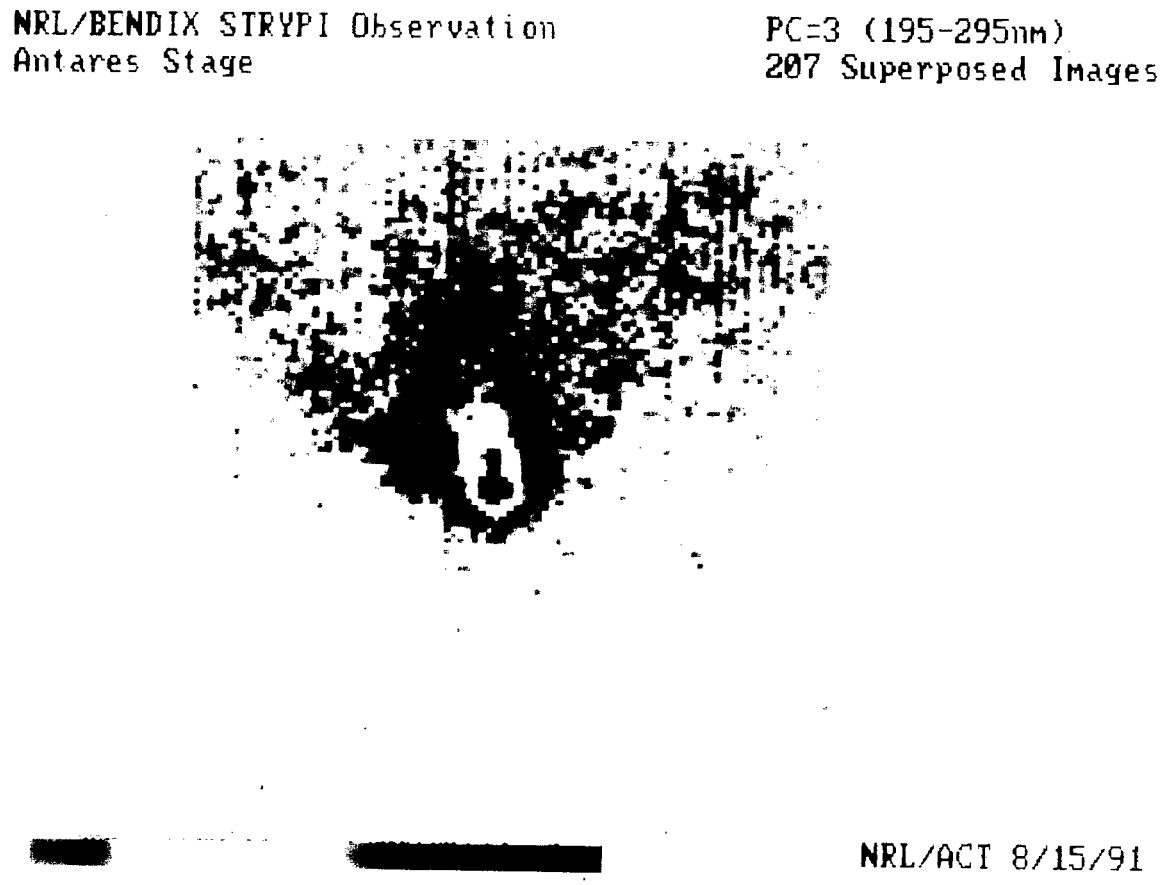

Fig. 11 - Composite plume-camera image

Table 10 - Centroid Statistics for Plume-Camera Images

Composite image	Images superposed	Angle variation (deg)	Centroid RMS jitter (pixels)	Average centroid position (row, column)
1	12	0	1.1	(55.6,41.2)
2	207	3.4	7.1	(48.8,40.4)
3	157	2.9	6.8	(52.5,42.5)
4	104	0.6	3.1	(52.8,42.4)

Figure 12 illustrates the effect of frame registration for interval 2 of the Strypi mission. The left image is obtained by using direct superposition; the right image is the result when using frame registration to remove smearing. Frame registration was done by rotating the consecutive images around the centroid point before they were superposed. The amount of rotation used was calculated by using rocket orientation data. In this case, the rotation angle was about 10°, and the effect of frame registration seems of minimal value. Generally, rotation has not been removed for rotation of 10° or less.

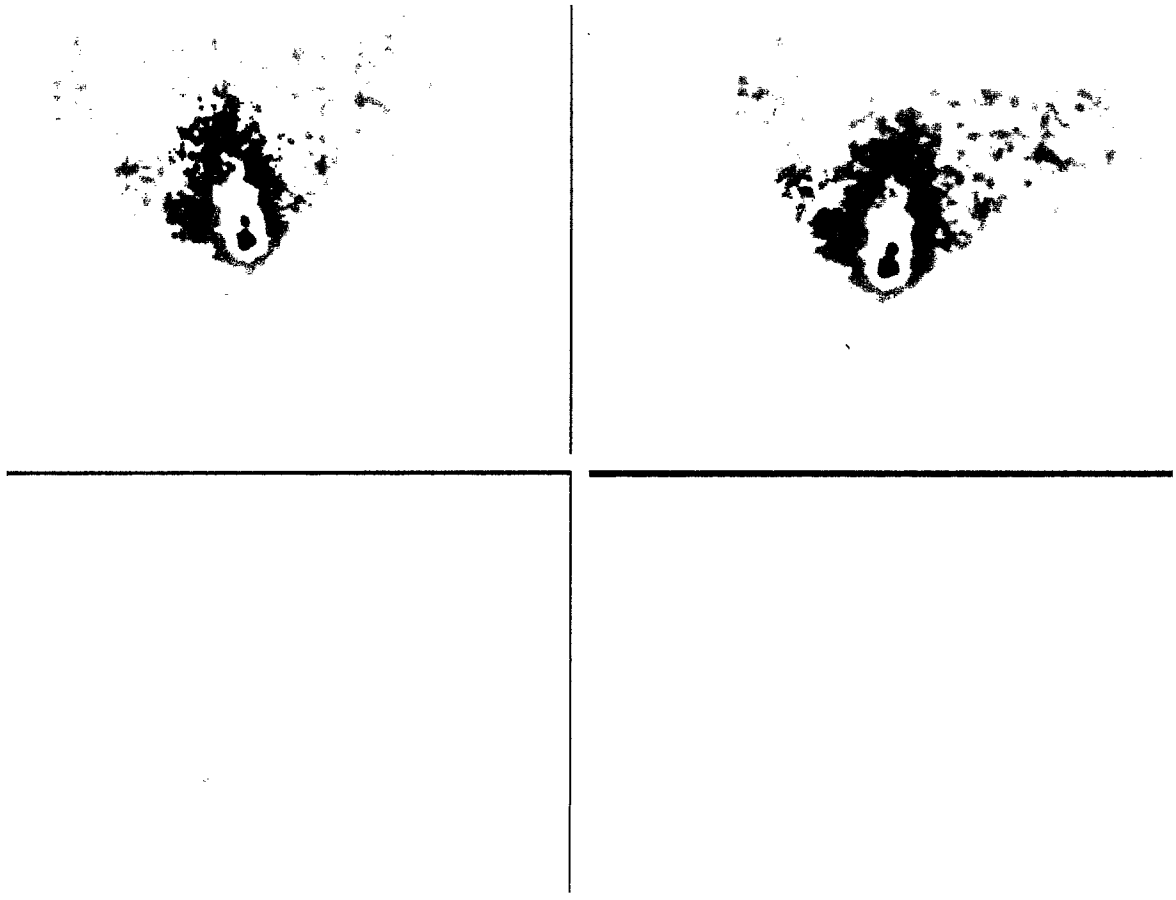

Fig. 12 - Comparison of image superposition methods. Left image uses direct superposition; right image uses frame registration.

4.0 EXTRACTION OF RADIOMETRIC QUANTITIES

Three levels of data reduction are useful for any radiometric experiment. In the first level, data are merely reduced to instrument readings or counts at the image plane. In the second level, instrument readings are converted by instrument specific factors (which may be approximate) into approximate measures of physical quantities (e.g., radiance, with no assumed spectral shape for the source being used). In the third level of reduction, a spectral shape is assumed to reduce data and present it.

A spectral shape must be assumed because instrument efficiency is a function of wavelength within each band. Because of this, the spectral distribution of incident photons is needed to provide the appropriate weighting at each wavelength within the pass band of integrated response. Since the spectral shape is not known from the data, a spectral shape must be assumed to determine this weighted distribution. Once a spectral shape has been assumed, the number of photoevents measured are used to infer the amplitude or intensity of that spectral shape.

4.1 Relation of Photoevents to Source Radiance

The UVPI gives data in the form of digitized numbers from the CCD. Photoevents at the image plane P_k are calculated from these numbers. This procedure was described in Section 2.

Presumably, the photoevents at the image plane are a result of a radiation source in the field of view. If the radiation source is isotropic and uniform over an emitting region of area A_S, then an expression for the photon flux ϕ_{in} incident on the face of the telescope in photons/second is:

$$\phi_{in} = (A_s \Omega_s / hc) \int \lambda L(\lambda) d\lambda , \tag{1}$$

where

$L(\lambda)$ is source spectral radiance in W/m^2-nm-sr,
A_s is area of emitting region,
Ω_s is solid angle of emission subtended by the telescope,
h is Planck's constant, and
c is speed of light.

The factor λ/hc converts the spectral radiance $L(\lambda)$ to a photon radiance (photons/s-m^2-nm-sr).

By setting the size of the emitting region equal to the footprint area of a pixel, the following reciprocity relation results:

$$A_s \Omega_s = A_s A_c / R^2 = A_c \Omega_p ,$$

where

A_C is system aperture area,
Ω_p is pixel field of view, and
R is range from the detector to the emitting region.

The general expression for the number of photoevents P_k in pixel k at the image plane resulting from an emitting source of spectral radiance $L(\lambda)$ filling the pixel field of view is then given by Ref. 7 as:

$$P_k = (A_c \Omega_p \tau / hc) \int \lambda Q(\lambda) L(\lambda) d\lambda , \tag{2}$$

where

τ is exposure time, and
$Q(\lambda)$ is wavelength-dependent photoelectronic conversion efficiency, or net quantum efficiency, of the optics and detector.

As an illustration, the number of photons per second incident on the face of the telescope ϕ_{in} and the number of photoevents P_k that would result from a blackbody source at 2300 K in the plume camera for filter PC-3 can be calculated by using Eqs. (1) and (2) where

$L(\lambda)$ is $L_{BB}(\lambda)=\frac{2hc^2}{\lambda^5}\frac{1}{\exp\left(\frac{hc}{\lambda kT}\right)-1}$ W/cm^2-sr-nm

$Q(\lambda)$ is quantum efficiency values given in Table 3 for PC-3
λ_1 is 195 nm
λ_2 is 295 nm
h is 6.624 x 10^{-34} J-s
c is 3.00 x 10^{17} nm/s
hc is 1.98 x 10^{-16} J-nm
k is 1.37 x 10^{-23} J/K
T is 2300 K

τ is .033 s
A_c is 78.5 cm^2
Ω_p is 1.28 x 10^{-10} sr
$A_c\Omega_p\tau$ is 3.32 x 10^{-10} cm^2-sr-s
$A_c\Omega_p$ is 1.00 x 10^{-8} cm^2-sr $= A_s\Omega_s$

$(1/hc)\int_{\lambda_1}^{\lambda_2}\lambda L(\lambda)d\lambda$ =7.43 x 10^{13} photons/s-cm^2-sr, and

$(1/hc)\int_{\lambda_1}^{\lambda_2}\lambda Q(\lambda)L(\lambda)d\lambda$ = 4.04 x 10^{10} photoevents/s-cm^2-sr.

Finally, this gives

ϕ_{in} = 7.43 x 10^5 photons/s, and
P_k = 13.4 photoevents.

In general, the exposure time τ is $^1/_{30}$th second for the plume camera. It is also variable to a maximum of $^1/_{30}$th second for the tracker camera. The pixel field of view Ω_p is 12.8 by 10.0 μrad = 1.28 x 10^{-10} sr for the plume camera, and 180.5 by 143.9 μrad = 2.6 x 10^{-8} sr for the tracker camera. At the typical range of 500 km, these pixel fields of view correspond to 6.4 by 5.0 m and 90 by 72 m, respectively.

For further insight into the relationship of photoevents to source radiance, several forms of approximation can be helpful. To begin, Eq. (2) can be rearranged as follows:

$$\int\lambda Q(\lambda)L(\lambda)d\lambda = P_k hc/\left(A_c\Omega_p\tau\right). \quad (3)$$

Now note that the integral on the left is similar to the source radiance integral, $\int L(\lambda)\,d\lambda$, except for the λ and $Q(\lambda)$ factors. One quick and simple approximation involves substituting constant

values for λ and $Q(\lambda)$; this allows them to come out from under the integral and move to the right side. For example, $\lambda_o = (\lambda_1 + \lambda_2)/2$ and $Q_o = Q_{max}/2$ provide estimated "average" values that allow reduction of the integral to an approximate radiance. Section 4.6 further discusses the sensitivity of these calculations to λ and $Q(\lambda)$ as well as different choices of assumed spectra. A more frequently used approximation, called the peak normalized radiance, is discussed in the next section.

4.2 The Peak Normalized Radiance Approximation

The second level of data reduction is to manipulate the instrument-specific factors to obtain approximate measures of physical quantities. One common method is called peak normalization in which both sides of Eq. (3) are divided by the quantities λ_m and $Q(\lambda_m)$. The definition of λ_m is given as the wavelength of peak net quantum efficiency, and $Q(\lambda_m)$ is the peak net quantum efficiency [8]. The result is called the peak normalized radiance L_{pn}, which is defined by:

$$L_{pn} = \int \lambda Q(\lambda) L(\lambda) d\lambda / \lambda_m Q(\lambda_m). \tag{4}$$

In practice, the evaluation of L_{pn} is based on the measured P_k, using:

$$L_{pn} = (P_k/\tau)\left(hc/\lambda_m Q(\lambda_m) A_c \Omega_p\right) \tag{5}$$

The values of λ_m, $Q(\lambda_m)$, and $\lambda_m Q(\lambda_m)$ for each of the filters are given in Table 11 and the quantity $hc/A_c\Omega_p = 1.88 \times 10^{-8}$ J-nm/cm^2-sr.

Table 11 - Peak Quantum Efficiency Parameters

Filter	λ_m (nm)	$Q(\lambda_m)$	$\lambda_m Q(\lambda_m)$ (nm)
Plume PC-1	270	.00606	1.64
Plume PC-2	305	.00182	0.555
Plume PC-3	250	.00284	0.710
Plume PC-4	280	.0131	3.67
Tracker	355	.0200	7.10

Even though Eq. (4) is an exact expression, it is not a true radiance because the integral contains terms other than $L(\lambda)$. L_{pn} approaches the true radiance as $[\lambda Q(\lambda)/\lambda_m Q(\lambda_m)]$ approaches 1. For UVPI, λ/λ_m is usually about equal to 1, but $Q(\lambda)/Q(\lambda_m) << 1$ for efficiency curves like PC-1 and PC-3 with long, low wings. On the other hand, efficiency curves for PC-2 and the tracker camera are more box-like and $Q/Q(\lambda_m)$ is close to one. This is discussed further in Section 4.6.

For illustration, Table 12 presents peak normalized radiance values and reference spectrum values obtained from an observation of an Antares rocket stage based on estimated P_k for the brightest pixel only. The ratio of the two radiances is included and compared in the last column. The peak normalized radiance underestimates the reference spectrum result by a factor of 5 or more for filters PC-1 and PC-3. These filters in particular have low efficiency wings. On the other hand, the L_{pn} is only down about a factor of 2 on PC-2 and the tracker.

Table 12 - P_k/τ and L_{pn} for Brightest Pixel

Filter	P_k/τ (PE/s)	L_{pn} (μW/sr-cm^2)	L_e (μW/sr-cm^2)	L_{pn}/L_e
Plume PC-1	26.1	0.32	2.57	0.12
Plume PC-2	10.8	0.39	0.70	0.56
Plume PC-3	6.7	0.19	0.90	0.21
Plume PC-4	162.0	0.88	3.08	0.29

Thus, the peak normalized radiance is an approximate measure of the total radiance in the passband of the filter and is usually a better approximation if the instrument response curves are near box-like rather than bell-shaped. Of course, a correct radiance can be obtained for any instrument response curve if the true spectrum is known and used to evaluate the integral in Eq. (4). In general, to gain a better estimate of the true in-band radiance, the shape of the plume spectrum must be known or estimated.

4.3 Reference Spectrum for Aluminum-Loaded Propellants

The third level of data reduction begins with the assumption of a spectral shape for the observed emission. The amplitude of the assumed spectrum plays no role, but the shape acts as a weighting function within the passband to determine the distribution of photons as a function of wavelength. This is important because the instrument efficiency is different at each wavelength within a passband, and thus, the implied photon flux at the telescope face for a fixed measurement of photoevents P_k depends on how the photons are distributed across that wavelength interval. What is needed is the spectral shape. Such a spectral shape is not directly provided by this instrument. Fortunately, previous measurements and theoretical models can aid in making a good assumption of the spectral shape, as explained below. The relative insensitivity of the resulting radiometric numbers to several different spectral shapes is discussed in Section 4.5.

The solid rocket motors under consideration contain powdered aluminum in their propellant. The aluminum oxidizes and emerges as an incandescent mist in the rocket exhaust. It is this mist of oxidized aluminum particles or droplets that emits much of the UV radiation seen by UVPI in the plume central region. The mist is optically thin, and the plumes are, thus, partially transparent. Because the heat of fusion for aluminum oxide is very high, and the rate of cooling for micron-sized particles is relatively low, the particles remain at approximately the melting temperature throughout the length of the plume. Thus, most of the light in the plume will be from this nearly transparent cloud of micron-sized Al_2O_3 particles at the melting point, 2320 K.

The assumed spectral shape that is used is that of a 2300 K blackbody times an emissivity function $\varepsilon_{Al}(\lambda)$ shown in Fig. 13 [9]. This emissivity curve is basically characteristic of hot alumina particles of the size found in rocket exhaust plumes [10].

The resulting normalized spectral shape is fairly generic to all solid fueled boosters with aluminum-loaded fuel and is termed the reference spectrum $R(\lambda)$. Mathematically,

$$R(\lambda) = \varepsilon_{Al}(\lambda) L_{BB}(\lambda), \tag{6}$$

where $L_{BB}(\lambda)$ is the 2300 K blackbody spectrum. The reference spectrum, compared to a blackbody spectrum, is shown in Fig. 14.

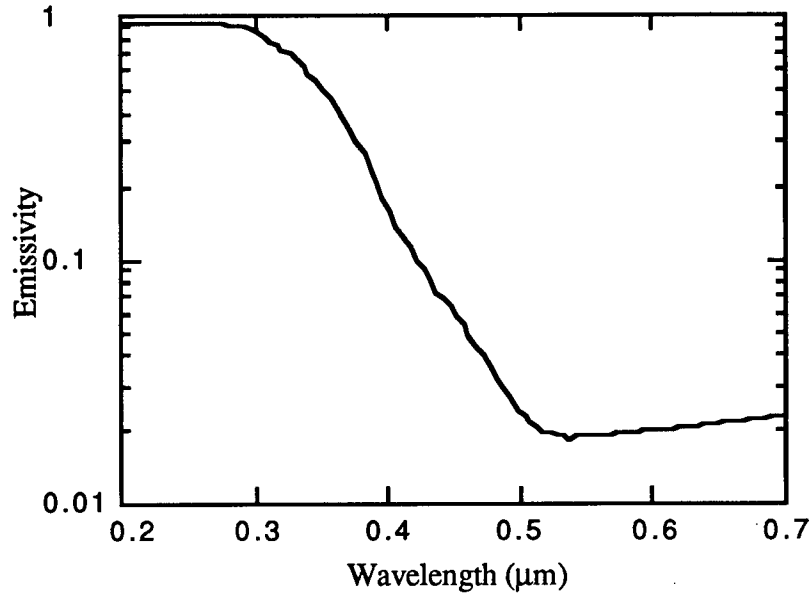

Fig. 13 - An emissivity curve for plume aluminum particles (2.3 μm)

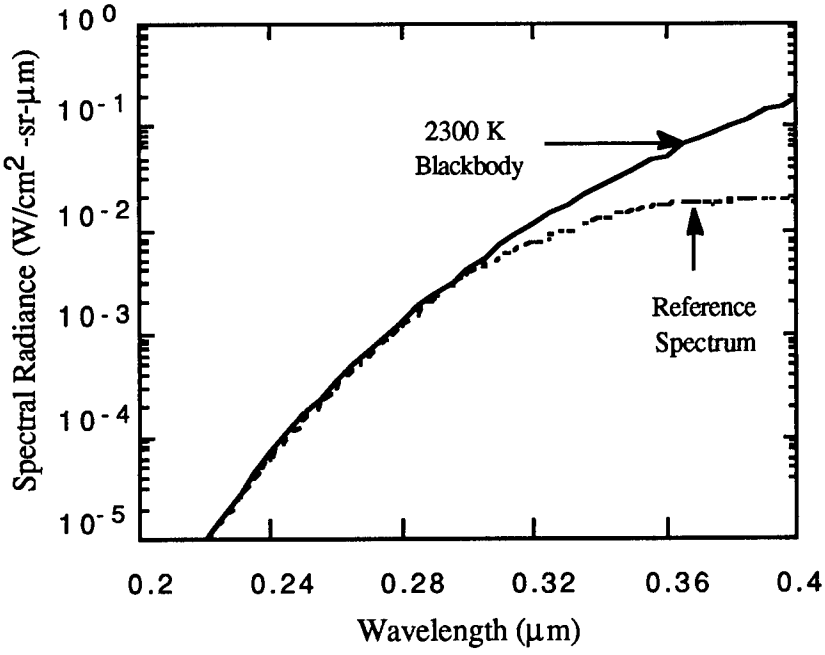

Fig. 14 - Assumed reference spectrum

The spectral shape is a good approximation to actual rocket plume spectra as verified by on-board spectrometers looking back into a rocket plume [11]. The actual spectra obtained by the spectrometers, shown in Fig. 15, is for the Antares and Star 27 motors on the Strypi mission. The line of sight is 4° from the rocket motor axis, looking back into the plume. As can be seen, the spectra of the two different motors look very similar in shape, and both match a 2320 K blackbody spectral shape below 300 nm, as does the reference spectral shape. Note that the blackbody curve in Fig. 15 has been scaled in spectral radiance by a factor of 20 while the blackbody curve in Fig. 14 has not. The agreement between Antares and Star 27 data is significant because the motors were of significantly different size and had very different fuel compositions. The Antares had an aluminized

double-base propellant, whereas the Star 27 was a more standard aluminum-ammonium perchlorate-rubber composite. The fact that they both gave measured spectra quite similar to the reference spectrum supports the concept that plume spectra for rockets with aluminized fuel exhibit a generic spectral shape that is insensitive to rocket motor size and detailed fuel composition and should resemble that of the reference spectrum. The on-board spectrometer and the UPVI have very different lines of sight. However, the spectral shape of the plume spectra should be insensitive to the detector line of sight through the plume. The data are quite consistent with the reference spectrum. Furthermore, sensitivity to the choice of spectrum is not overly acute, as is shown in Section 4.6 for several sample spectra.

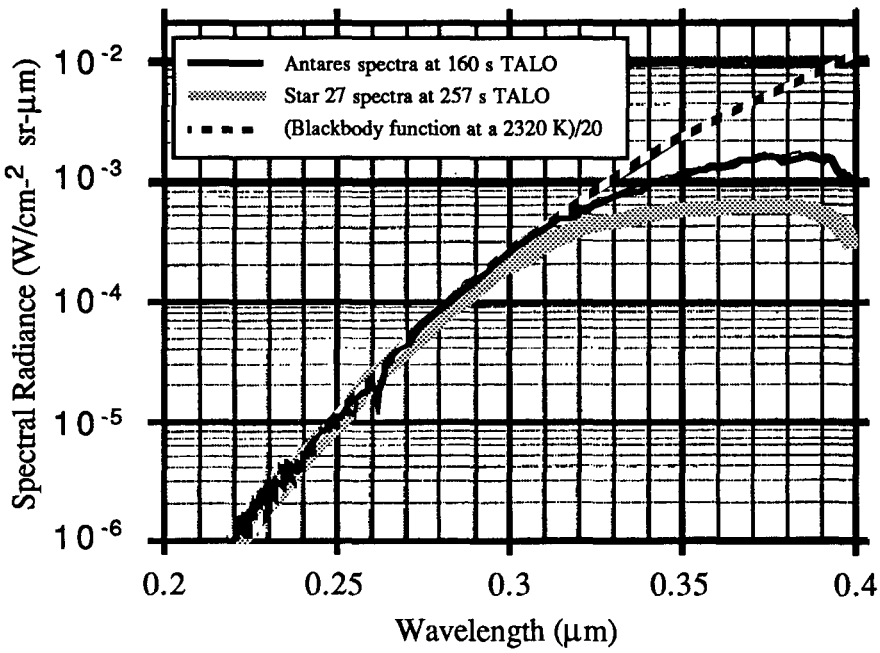

Fig. 15 - On-board spectrometer measurement for Strypi mission

4.4 Use of the Reference Spectrum to Calculate a Scaling Constant

Assuming that the reference spectrum $R(\lambda)$ gives the proper spectral shape for $L(\lambda)$ is equivalent to saying that $L(\lambda)$ and $R(\lambda)$ are related by a scaling constant α, which is independent of λ:

$$\alpha = L(\lambda)/R(\lambda). \tag{7}$$

The scaling factor α_K for a pixel can be obtained by first calculating the number of photoevents, P_k' expected for the unscaled reference spectrum, using the expression

$$P_k' = \left(A_c \Omega_p \tau / hc\right) \int \lambda Q(\lambda) R(\lambda) d\lambda, \tag{8}$$

and then using the ratio of Eq. (2) to Eq. (8), namely,

$$\frac{P_k}{P_k'} = \frac{\int \lambda Q(\lambda) L(\lambda) d\lambda}{\int \lambda Q(\lambda) R(\lambda) d\lambda} = \frac{\alpha \int \lambda Q(\lambda) R(\lambda) d\lambda}{\int \lambda Q(\lambda) R(\lambda) d\lambda} = \alpha_K, \tag{9}$$

where the calculated value of P_k' is the same for all k (i.e., k in P_k' is superfluous).

Therefore, α_K can be calculated for each passband and for each pixel by calculating P_k' and comparing it to the measured value of P_k:

$$\alpha_\kappa = P_k / P_k', \tag{10}$$

which gives an in-band, effective value of α_K for that pixel. Actually, these plumes are optically thin, and α_K, in some sense, provides a measure of that thinness or density of emitters along that pixel's line of sight.

After α_K is known, the source spectral radiance function $L(\lambda)$ can be calculated by using Eq. (7) and, in turn, can be used to calculate in-band total radiance for the plume data in various filter bandpasses. All the radiometric values presented in this report can be obtained from the source function $L(\lambda)$ defined by Eqs. (7) and (10).

As a practical example, Table 13 shows the values of P_k/τ and P_k'/τ obtained as averages for the brightest pixel over several frames for the Antares plume together with the ratios of P_k to P_k' for the four plume-camera filter bands. The reference spectrum varies over more than three orders of magnitude in the region of the filter bands, while the values of α_K for the four filter bandpasses are all within a factor of four. Additionally, the fact that these values for α_K are 5 to 9 times smaller than the .05 value for α_K obtained with the on-board spectrometer is in good agreement with the smearing by the point spread function expected for the brightest pixel. See Section 5.2 regarding expected smearing by the point spread function. All this suggests that the reference spectrum is a reasonable approximation to the actual plume spectral shape.

Table 13 - Scaling Constant Calculation Using Antares Plume Data

Filter	P_k/τ (PE/s)	P_k'/τ (PE/s)	α_K
Plume PC-1	26.1	1810	.0144
Plume PC-2	10.8	1870	.0058
Plume PC-3	6.7	355	.0189
Plume PC-4	162.0	27200	.0060

4.5 Centroid Wavelength Determination and Photon Energy

The procedure described above yields a spectral radiance function $L(\lambda)$, described by a scaling factor and an assumed spectral shape. Because these radiance functions are rapidly varying functions of λ, a wide spread of spectral radiance values is usually associated with each waveband. It is, however, usually convenient and desirable to provide single numerical values of plume spectral radiance and spectral radiant intensity for a waveband. This can be achieved simply by taking $L(\lambda)$ of Eq. (7) at a specific, chosen wavelength within each filter passband. This wavelength could be selected to be the center of each filter passband, but this choice would neglect the shift in the effective measurement resulting from the source spectrum and instrument response function. For UVPI, a response centroid wavelength, weighted by the reference spectral function, is defined:

$$\lambda_c \equiv \int \lambda^2 R(\lambda) Q(\lambda) d\lambda \Big/ \int \lambda R(\lambda) Q(\lambda) d\lambda . \tag{11}$$

This is the wavelength at which the predominant photoevent response occurs for each spectrum/filter combination. Centroid wavelengths were computed for several spectral shapes,

including the reference spectral shape, and are shown in Table 14. Here the integrals of Eq. (11) have been evaluated as discrete summations over each bandpass using the limits given in Table 2. Note that the rounded centroid wavelength values shown in Table 14 for the reference spectrum are the values actually used in the data reduction process.

Table 14 - Centroid Wavelength for Various Spectra

	PC-3 (nm)	PC-1 (nm)	PC-2 (nm)	PC-4 (nm)	Tracker (nm)
1800 K blackbody	270.4	282.4	310.0	314.1	416.2
2300 K blackbody	265.8	279.2	309.7	308.5	409.7
Reference spectrum (rounded)	265.8 (265)	279.1 (280)	309.6 (310)	306.4 (305)	389.4 (390)
Flat spectrum	248.1	270.7	309.0	287.3	369.5
Peak normalized	250.0	270.0	310.0	280.0	355.0

This is simply a means of selecting a nominal characteristic wavelength for each spectral shape for which a single numerical spectral radiance value can be reported as representative of that measurement. Other approaches might have been used to select a reference wavelength for describing the spectral radiance function. As mentioned above, one might, for example, have selected the central wavelength of each filter as the place for citing the "representative" numerical value of spectral radiance. This would yield different values for the spectral radiances without changing the function $L(\lambda)$ at all. Thus, when single numerical values are used for reporting spectral radiometric parameters, they must be treated with care, and special attention must be given to the wavelength chosen for representing that waveband.

The photon energy at the centroid wavelength E_c can also be calculated by using the expression:

$$E_c = hc/\lambda_c .$$

Table 15 shows these energies for several assumed spectra. The spread in the normalization factors shown in parentheses indicates a rather tight grouping of the photon energies regardless of assumed spectra. Such insensitivity to spectral shape is discussed more in the next section.

Table 15 - Photon Energy at λ_c for Assumed Spectra

	PC-3 (J/photon)	PC-1 (J/photon)	PC-2 (J/photon)	PC-4 (J/photon)	Tracker (J/photon)
1800 K blackbody	7.04×10^{-19} (0.99)	6.50×10^{-19} (0.99)	6.38×10^{-19} (1.00)	6.05×10^{-19} (0.98)	4.71×10^{-19} (0.92)
2300 K blackbody	7.12×10^{-19} (1.00)	6.60×10^{-19} (1.00)	6.40×10^{-19} (1.00)	6.13×10^{-19} (0.99)	4.80×10^{-19} (0.94)
Reference spectrum	7.12×10^{-19} (1.00)	6.59×10^{-19} (1.00)	6.40×10^{-19} (1.00)	6.19×10^{-19} (1.00)	5.11×10^{-19} (1.00)
Flat spectrum	8.09×10^{-19} (1.14)	7.39×10^{-19} (1.12)	6.48×10^{-19} (1.01)	6.97×10^{-19} (1.13)	5.51×10^{-19} (1.08)
Peak normalized	7.95×10^{-19} (1.12)	7.33×10^{-19} (1.11)	6.52×10^{-19} (1.02)	7.10×10^{-19} (1.15)	5.60×10^{-19} (1.10)

4.6 Sensitivity to Different Spectral Assumptions

The effect of different spectral assumptions can be compared by calculating, for each waveband/spectrum combination, the implied incident photon flux at the face of the telescope per photoevent recorded at the image plane. Then, values are compared for a waveband. This was done by using Eq. (12) below, which was obtained by multiplying Eq. (1) by τ, the exposure time, and then dividing by Eq. (2). That is:

$$\tau\phi_{in}/P_k = \int \lambda L(\lambda)d\lambda \Big/ \int \lambda Q(\lambda)L(\lambda)d\lambda, \tag{12}$$

where multiplication by τ yields units of photons/photoevent.

Table 16 shows the result of the calculation. The table is arranged so that each column gives results for one of the UVPI wavebands, starting with the shortest wavelength band (PC-3) on the left, and progressing to longer wavelengths on the right. Each of rows 1 through 4 gives results for the designated spectrum, i.e., 1800 K blackbody, 2300 K blackbody, reference spectrum, and flat spectrum, respectively. Row 5 gives the peak normalized approximation result. The numbers in parentheses provide a comparison ratio of the values within a column where the reference spectrum has been assigned the value 1. The rows have been arranged to show the flattest spectra in the lower rows of the table and the more steeply inclined (toward long wavelengths) spectra in the upper rows.

Each entry in the table may be viewed as the inverse of an "average" efficiency. This is clear from a comparison of Eq. (12) to the defining expression for the average efficiency $\overline{Q}$ in each waveband:

$$\overline{Q} = \int Q(\lambda)\lambda L(\lambda)d\lambda \Big/ \int \lambda L(\lambda)d\lambda, \tag{13}$$

where $\lambda L(\lambda)$, the photon distribution, serves as a weighting function in the calculation of the average and the units are in photoevents/photon.

Table 16 - Implied Incident Flux for Assumed Spectra*

	PC-3 (photons/PE)	PC-1 (photons/PE)	PC-2 (photons/PE)	PC-4 (photons/PE)	Tracker (photons/PE)
1800 K blackbody	2600 (1.40)	2690 (1.76)	1040 (1.06)	463 (1.54)	81.9 (1.14)
2300 K blackbody	1840 (1.00)	1620 (1.07)	996 (1.02)	344 (0.95)	75.3 (1.07)
Reference spectrum	1840 (1.00)	1510 (1.00)	976 (1.00)	294 (1.00)	66.2 (1.00)
Flat spectrum	838 (0.52)	625 (0.46)	918 (0.95)	165 (0.63)	74.1 (1.21)
Peak normalized	352 (0.19)	165 (0.11)	551 (0.56)	76.2 (0.26)	50.0 (0.76)

*Note: not redleak corrected

When reading up the columns, the table entries show a definite trend toward increasing values. Thus, the trend when reading up the column is one of *decreasing* average efficiency. This decrease is less pronounced in PC-2 and the tracker camera than in the other wavebands. The sensitivity to spectral choice is different for the different wavebands. This is largely due to the different shapes of

the net quantum efficiency curves. Three of the curves shown in Section 1.3, those for PC-1, PC-3, and PC-4, are bell-shaped, and the efficiency rolls off rather steeply from the peak down onto long, low wings. PC-2 and the tracker-camera curves are more flat-topped. By using the centroid wavelength information given in Section 4.5 for each band, one can locate that wavelength point on the efficiency curves of Section 1.3. For the three bell-shaped cases, the efficiency slides down to lower and lower values as the spectra (and centroid wavelength) favor longer and longer wavelengths. On the other hand, for the flat-topped spectra of PC-2 and the tracker camera the efficiency simply slides along the flat top with little change. For example, the first four rows of centroid wavelength values from Table 14 for the tracker camera vary from about 370 to 416 nm. This corresponds to only a 20% change in average efficiency, while a similar change in PC-1 from 270 to 282 nm produces a 300% change.

For the worst-case bell-shaped efficiency curves, the sensitivity to different spectral assumptions is within a factor of 2 if the 1800 K blackbody assumption is ignored. The spectral results of all of the rocket observations and the on-board Strypi spectrometer so far analyzed show results that are as flat as, or flatter than, a 2300 K blackbody. Overall, the sensitivity is not acute for spectra of only modest slope differences.

The Peak Normalized Approximation has been left out of the discussion thus far because it does not actually use an assumed spectrum. The average efficiency is replaced by Q_{max}, which is generally 2.5 to 5.0 times the average efficiency of a bell-shaped efficiency curve and 1.5 to 2.0 times that of a flat-topped efficiency curve. As such, Q_{max} provides a rather mediocre approximation; actually, $Q_{max}/2$ would have been better.

Table 17 provides the implied energy flux in joules per photoevent. Note, this is the total input energy to produce one photoevent, not the average energy of one input photon. The values show a factor of two difference in sensitivity for the three key spectra. This is similar to the results shown in Table 16.

Table 17 - Implied Incident Energy for Several Assumed Spectra*

	PC-3 (J/PE)	PC-1 (J/PE)	PC-2 (J/PE)	PC-4 (J/PE)	Tracker (J/PE)
1800K blackbody	1.83×10^{-15} (1.40)	1.75×10^{-15} (1.76)	6.64×10^{-16} (1.06)	2.80×10^{-16} (1.54)	3.86×10^{-17} (1.14)
2300K blackbody	1.31×10^{-15} (1.00)	1.07×10^{-15} (1.08)	6.38×10^{-16} (1.02)	2.11×10^{-16} (1.16)	3.61×10^{-17} (1.07)
Reference spectrum	1.31×10^{-15} (1.00)	9.95×10^{-16} (1.00)	6.26×10^{-16} (1.00)	1.82×10^{-16} (1.00)	3.38×10^{-17} (1.00)
Flat spectrum	6.78×10^{-16} (0.52)	4.62×10^{-16} (0.46)	5.94×10^{-16} (0.95)	1.15×10^{-16} (0.63)	4.08×10^{-17} (1.21)
Peak normalized	2.80×10^{-16} (0.21)	1.21×10^{-16} (0.12)	3.59×10^{-16} (0.57)	5.41×10^{-17} (0.30)	2.80×10^{-17} (0.83)

* Note: not redleak corrected

4.7 Calculations of Radiance and Radiant Intensity

Once the spectral radiance is known, the spectral integrals can be evaluated to obtain values for the radiance:

$$L_e \equiv \int_{\lambda_L}^{\lambda_U} L(\lambda)d\lambda = \alpha \int_{\lambda_L}^{\lambda_U} R(\lambda)d\lambda . \qquad (14)$$

The units of L_e are (power)/(area)(solid angle), or W/m^2-sr. The evaluation of these integrals is limited to the nominal bandwidth of the pertinent filter. Note that the integrand of Eq. (14) does not include the response function $Q(\lambda)$, and, therefore, does not become small outside the filter passbands. This means the values obtained for L_e will depend very strongly on the limits of integration.

Radiance and spectral radiance are most useful for comparing the observed signals from diffuse phenomena with fairly uniform distributed emission, e.g., airglow, scattered sunlight, or scattered moonlight. For some observations, such as peaked spatially localized sources, the radiant intensity and spectral radiant intensity are useful. These quantities, when taken over the pixel region covering the source, contain the correct total radiant intensity whereas radiance measurements usually associated with a pixel can be distorted by the point spread function. In the case of the tracker camera, a plume may be only partially resolved and fill only part of a pixel. Radiance values based on the full pixel size are then erroneous. Conversion to radiant intensity can be achieved from the preceding expressions by multiplying by $R^2\Omega_p$, where R is the range to the source and Ω_p is the pixel field of view. The result is then summed over the pixels that contain signal. This is equivalent to summing the apparent radiance or spectral radiance over the projected pixel footprint area and attributing it to a point source within the field of view of the pixel. The spectral radiant intensity $I(\lambda)$ and the radiant intensity I_e can be obtained directly from the corresponding expressions for the spectral radiance and radiance, Eqs. (7) and (14), respectively:

$$I(\lambda) = R^2\Omega_p L(\lambda) = R^2\Omega_p \alpha R(\lambda), \tag{15}$$

and

$$I_e \equiv \int_{\lambda_L}^{\lambda_U} I(\lambda)d\lambda = R^2\Omega_p L_e. \tag{16}$$

The units of $I(\lambda)$ are (power)/(spectral bandwidth)(solid angle), or W/nm-sr, and the units of I_e are (power)/(solid angle), or W/sr. As with the radiance, the radiant intensity is an integral across a limited portion of the spectrum defined by the band edges. Again, the integrands do not include the response function $Q(\lambda)$ and thus, are not small at the band edges. This means the values are very sensitive to the limits of integration chosen.

4.8 Recap of Radiometric Extraction and Conversion Constants

The essence of the radiometric extraction methodology is the determination of the amplitude of the reference spectral shape that would yield the observed photoevent count. If some emission phenomenon should be discovered that features a different emission spectral shape, the analyses would necessarily change, and different values for the nominal spectral radiance of the source would result. This is a well-known and unavoidable problem in the interpretation of radiance measurements.

The principal results of the analysis are (a) the source spectral radiance function $L(\lambda)$ expressed in terms of a scalar α and an assumed spectral shape function, and (b) the spectral radiant intensity function $I(\lambda)$. These functions may vary rapidly with wavelength.

Nominal spectral radiance values needed for displays of the measurements are obtained by: (a) specifying a reference wavelength for each filter (the centroid wavelength), and (b) calculating the spectral radiance at that wavelength with the scaled spectral shape function. Changing the reference wavelengths would change the nominal values without changing the radiance source.

Radiance and radiant intensity values are obtained by integrating the scaled source spectral shape function between specified limits. The limits chosen here are the nominal bandpass limits of the various filters (defined in Table 2). Any change in these limits will correspondingly change the values, even though the source spectrum and strength are unchanged. These numbers are very sensitive to the limits of integration and can be compared to any other numbers only if the other values are based on identical spectral limits.

Table 18 summarizes the definitions of conversion constants most often encountered in calculating one radiometric quantity from another. Table 19 gives the specific values for the conversion constants based on the assumed reference spectrum. Any revised spectral shape assumption will lead to a different set of conversion coefficients. Table 20 lists the radiometric values that correspond to one photoevent per second using the constants in Table 19. The radiant intensity values refer to a range of 500 km. The spectral radiance $L(\lambda_c)$ and the radiance L_e values are based on a single photoevent per second per pixel. Any arbitrary number of photoevents measured in a particular pixel is multiplied by the value in the table to determine the radiance of the source in that pixel's field of view. The spectral radiant intensity $I(\lambda_c)$ and radiant intensity I_e values are per pixel, even though these terms are used more often to refer to the total number of photoevents measured in the entire plume image.

Table 18 - Summary of Formulas Defining Conversion Constants

From	To	Op	Formula
P_k/τ (photoevents/s)	ϕ_{in} (photons/s)	x C_1	$C_1 = \frac{\int \lambda R(\lambda) d\lambda}{\int \lambda R(\lambda) Q(\lambda) d\lambda}$
ϕ_{in} (photons/s)	P_{in} (W)	x C_2	$C_2 = \frac{hc \int R(\lambda) d\lambda}{\int \lambda R(\lambda) d\lambda}$
P_{in} (W)	I_e (W/sr)	÷C_3	$C_3 = A_c / R^2$
L_e (W/sr-cm^2) I_e (W/sr)	$L(\lambda_c)$ (W/cm^2-sr-nm) $I(\lambda_c)$ (W/sr-nm)	+C_4	$C_4 = \frac{\int \lambda L(\lambda) d\lambda}{L(\lambda_c)}$
I_e (W/sr) $I(\lambda_c)$ (W/sr-nm)	L_e (W/cm^2-sr) $L(\lambda_c)$ (W/cm^2-sr-nm)	+C_5	$C_5 = R^2 \Omega_p$

Table 19 - Conversion Constants for the Reference Spectrum

Constant	Units	PC-3	PC-1	PC-2	PC-4	Tracker
C_1	photons/PE	1840	1510	976	294	66.2
C_2	J/photon	9.11 x 10^{-19}	6.61 x 10^{-19}	6.41 x 10^{-19}	6.19 x 10^{-19}	5.11 x 10^{-19}
C_3	steradians	3.12 x 10^{-14}	3.12 x 10^{-14}	3.12 x 10^{-14}	3.12 x 10^{-14}	3.12 x 10^{-14}
C_4	nm	104.5	150.2	20.4	105.5	125.2
C_5	cm^2	31.9 x 10^4	31.9 x 10^4	31.9 x 10^4	31.9 x 10^4	6510 x 10^4

Table 20 - Radiometric Values for One Photoevent Per Second

	PC-3	PC-1	PC-2	PC-4	Tracker
P_k/τ (photoevents/s)	1	1	1	1	1
ϕ_{in} (photons/s)	1840	1510	976	294	66.2
P_{in} (W)	1.31 x 10^{-15}	9.95 x 10^{-16}	6.26 x 10^{-16}	1.82 x 10^{-16}	3.38 x 10^{-17}
I_e (W/sr)	4.16 x 10^{-2}	3.17 x 10^{-2}	1.99 x 10^{-2}	5.80 x 10^{-3}	1.08 x 10^{-3}
$I(\lambda_c)$ (W/sr-nm)	3.96 x 10^{-4}	2.11 x 10^{-4}	9.76 x 10^{-4}	5.50 x 10^{-5}	8.60 x 10^{-6}
L_e (W/sr-cm^2)	1.43 x 10^{-7}	1.09 x 10^{-7}	6.82 x 10^{-8}	1.98 x 10^{-8}	1.73 x 10^{-11}
$L(\lambda_c)$ (W/sr-cm^2-nm)	1.36 x 10^{-9}	7.24 x 10^{-10}	3.34 x 10^{-9}	1.88 x 10^{-10}	1.38 x 10^{-13}

5.0 POINT SPREAD FUNCTION AND ITS EFFECTS

The full-width-half-maximum of the plume-camera point spread function is about 90 microradians (9 pixels), and that of the tracker camera is about 230 microradians (1.5 pixels). The effect of the point spread is to blur a small source image over an increased image area, thereby reducing its apparent peak radiance as well as increasing its apparent dimensions. The amount of the reduction of the apparent source radiance depends on the true dimensions and radiometric shape of the source. These effects are significant in any comparison of the measured radiance values presented in image and contour plots with true or predicted values. Similarly, any determination of the source dimensions will be affected.

5.1 Point Spread Function

The effective UVPI point spread function (PSF) is defined as the response of the instrument to a point source, e.g., a star or a ground-based beacon. Figure 16 a shows a plume camera image of a ground-based beacon. A scaled version of the plume camera's PSF for the beacon is presented in Table 21. The intensity values were scaled such that the brightest pixel mapped to the value one. Figure 17 shows a three-dimensional plot of the PSF that results from observation of the ground-based beacon. For the ground-based beacon, the axial length of the PSF from peak to 50% of the peak along the major axis is about 4 pixels or 20 m at a range of 450 km, as shown in Fig. 18.

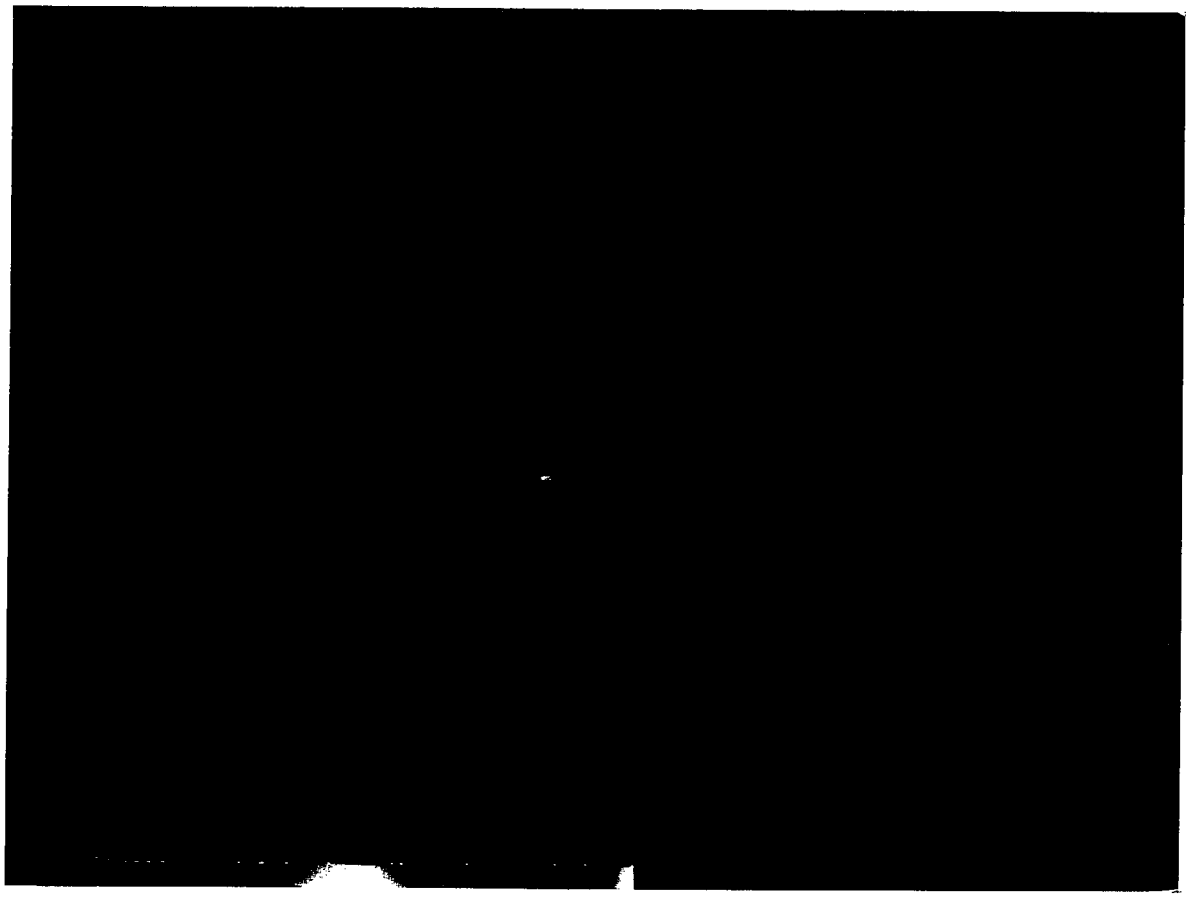

Fig. 16 - Plume-camera image of ground-based beacon

Figure 19 shows a tracker-camera image of a ground-based beacon. A scaled version of the tracker camera's PSF for the beacon is presented in Table 22. The intensity values were scaled such that the brightest pixel mapped to one. Figure 20 shows a three-dimensional plot of the PSF that results from observation of the ground-based beacon; Fig. 21 is an axial profile of the beacon as seen by the tracker camera.

Table 21 - Scaled Version of Plume Camera PSF

0.139	0.153	0.125	0.116	0.111	0.125	0.130	0.134	0.144	0.167	0.134	0.111	0.102	0.093	0.074	0.074
0.093	0.111	0.102	0.106	0.111	0.125	0.139	0.148	0.200	0.237	0.209	0.158	0.116	0.097	0.097	0.069
0.106	0.102	0.102	0.102	0.116	0.144	0.186	0.213	0.246	0.251	0.241	0.195	0.158	0.125	0.097	0.079
0.106	0.097	0.093	0.111	0.120	0.167	0.241	0.316	0.404	0.395	0.386	0.293	0.200	0.116	0.102	0.069
0.120	0.102	0.097	0.120	0.144	0.204	0.367	0.525	0.534	0.581	0.623	0.469	0.237	0.134	0.116	0.097
0.074	0.083	0.097	0.111	0.134	0.241	0.511	0.762	0.730	0.804	0.800	0.613	0.376	0.181	0.111	0.083
0.083	0.088	0.102	0.120	0.144	0.260	0.627	0.804	0.869	0.958	0.855	0.623	0.506	0.265	0.148	0.111
0.069	0.093	0.097	0.120	0.181	0.344	0.734	0.925	1.000	0.995	0.920	0.720	0.511	0.283	0.153	0.097
0.065	0.079	0.102	0.130	0.209	0.400	0.609	0.823	0.888	0.874	0.827	0.660	0.367	0.209	0.120	0.097
0.079	0.079	0.093	0.120	0.172	0.316	0.516	0.697	0.744	0.609	0.613	0.437	0.209	0.148	0.111	0.106
0.065	0.069	0.097	0.120	0.134	0.246	0.479	0.651	0.479	0.413	0.362	0.274	0.162	0.139	0.093	0.083
0.060	0.065	0.079	0.088	0.116	0.186	0.404	0.441	0.288	0.260	0.223	0.186	0.139	0.125	0.097	0.079
0.079	0.074	0.083	0.079	0.106	0.148	0.237	0.218	0.218	0.181	0.167	0.148	0.116	0.097	0.088	0.069
0.074	0.074	0.079	0.088	0.079	0.111	0.167	0.144	0.167	0.153	0.139	0.130	0.083	0.083	0.069	0.065
0.060	0.060	0.074	0.074	0.088	0.097	0.134	0.116	0.116	0.106	0.097	0.088	0.083	0.069	0.065	0.065
0.046	0.065	0.065	0.069	0.083	0.079	0.083	0.093	0.097	0.093	0.079	0.079	0.079	0.079	0.065	0.069

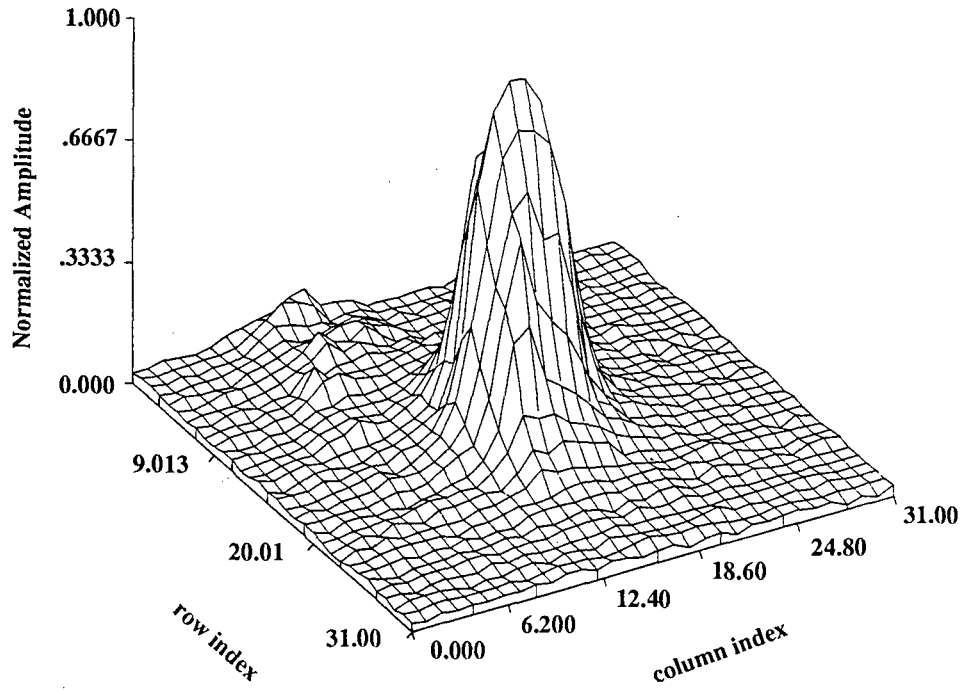

Fig. 17 - Plume-camera PSF for ground-based beacon

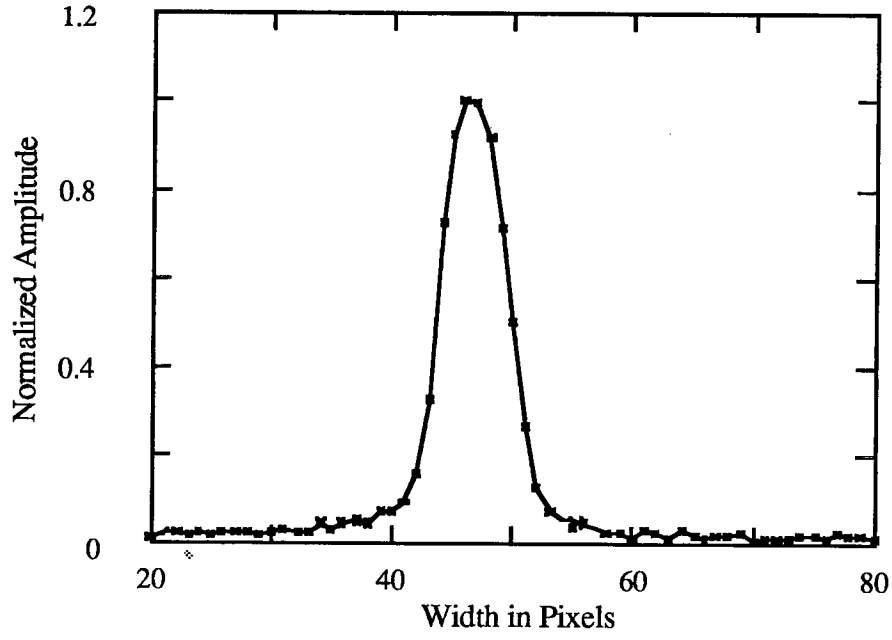

Fig. 18 - Axial profile through plume-camera PSF

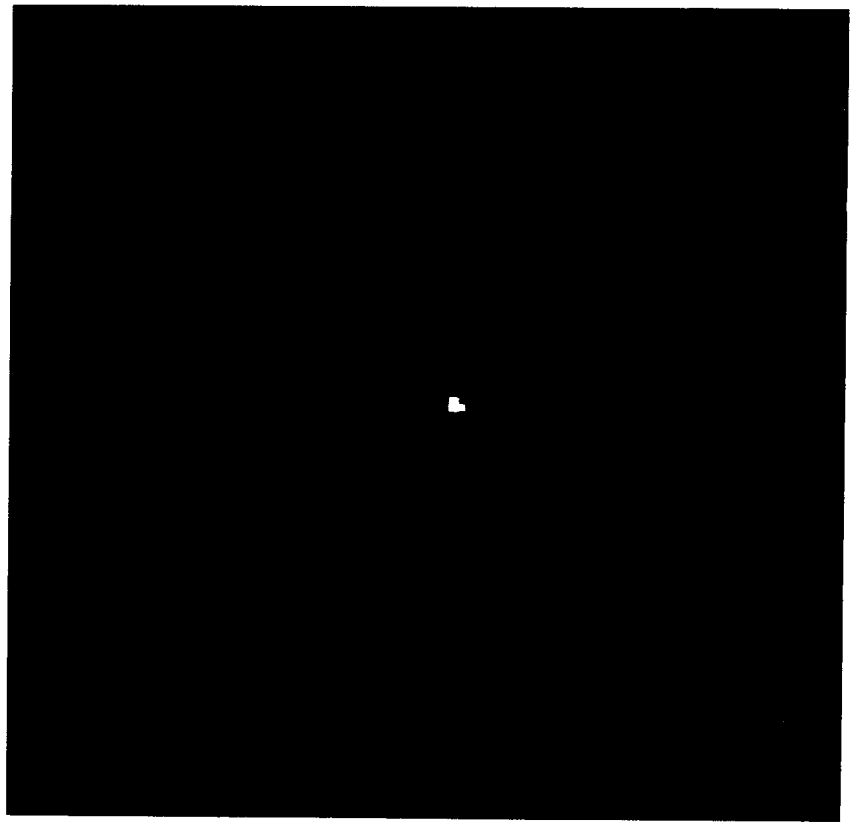

Fig. 19 - Tracker-camera image of ground-based beacon

Table 22 - Scaled Version of Tracker Camera PSF

0.036	0.041	0.036	0.023	0.037	0.039	0.034	0.036	0.030	0.024	0.036	0.001	0.036	0.008	0.047	0.021
0.012	0.035	0.017	0.026	0.037	0.034	0.039	0.019	0.032	0.008	0.051	0.003	0.042	0.000	0.029	0.025
0.047	0.016	0.018	0.027	0.043	0.026	0.036	0.033	0.022	0.013	0.058	0.034	0.024	0.035	0.027	0.032
0.044	0.024	0.028	0.052	0.035	0.052	0.054	0.024	0.034	0.016	0.037	0.032	0.028	0.061	0.037	0.041
0.045	0.033	0.034	0.038	0.029	0.047	0.015	0.064	0.049	0.036	0.082	0.028	0.042	0.028	0.068	0.015
0.045	0.001	0.061	0.028	0.063	0.059	0.054	0.057	0.083	0.056	0.061	0.017	0.042	0.029	0.036	0.026
0.036	0.058	0.043	0.060	0.047	0.050	0.074	0.126	0.108	0.042	0.027	0.036	0.043	0.026	0.046	0.033
0.037	0.028	0.026	0.041	0.055	0.049	0.212	0.986	0.511	0.081	0.069	0.051	0.033	0.026	0.027	0.015
0.050	0.032	0.037	0.052	0.037	0.087	0.227	1.000	0.535	0.092	0.076	0.034	0.016	0.044	0.010	0.030
0.053	0.017	0.036	0.027	0.021	0.051	0.055	0.141	0.105	0.055	0.067	0.040	0.026	0.032	0.021	0.097
0.010	0.032	0.032	0.059	0.025	0.049	0.070	0.075	0.039	0.040	0.035	0.032	0.036	0.036	0.021	0.032
0.030	0.030	0.036	0.016	0.027	0.050	0.034	0.042	0.039	0.022	0.046	0.031	0.037	0.017	0.029	0.015
0.028	0.025	0.034	0.020	0.053	0.030	0.059	0.029	0.039	0.042	0.053	0.052	0.036	0.043	0.045	0.026
0.046	0.034	0.042	0.042	0.042	0.025	0.045	0.051	0.056	0.018	0.036	0.018	0.013	0.029	0.037	0.041
0.043	0.027	0.026	0.023	0.044	0.041	0.036	0.028	0.066	0.027	0.033	0.035	0.053	0.035	0.053	0.040
0.042	0.031	0.027	0.056	0.061	0.024	0.055	0.027	0.040	0.015	0.040	0.027	0.028	0.028	0.037	0.017

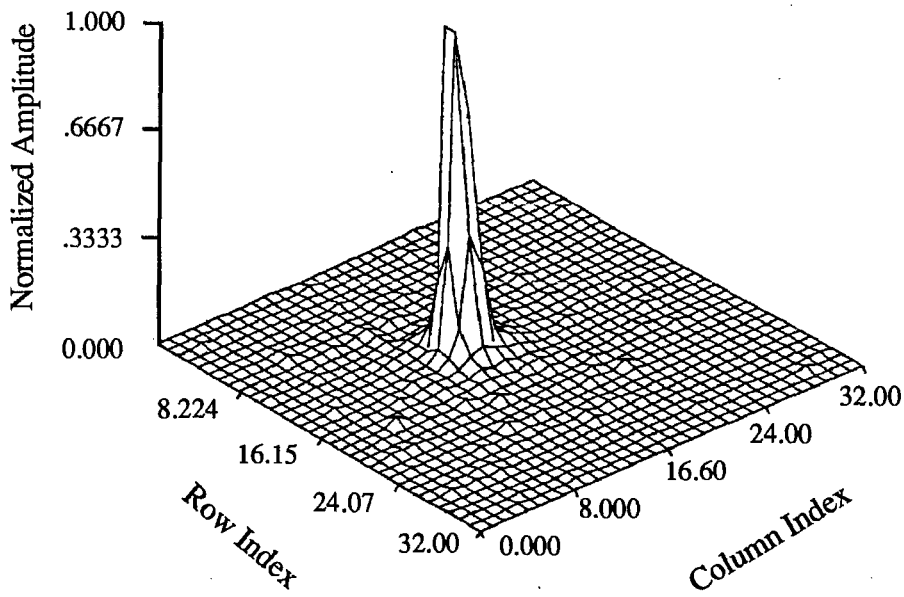

Fig. 20 - Tracker-camera PSF for ground-based beacon

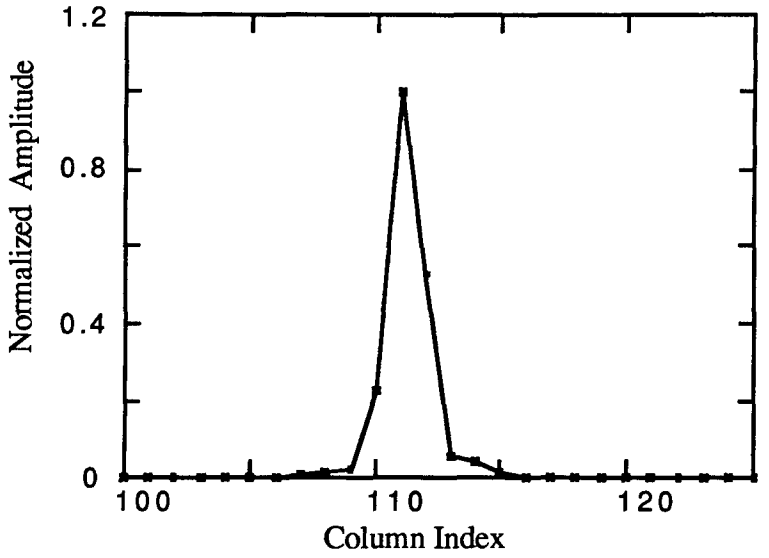

Fig. 21 - Axial profile through tracker-camera PSF

5.2 Effect on Peak Pixel Radiance

This subsection looks at the result of smearing a hypothetical high-resolution plume prediction by convolving it with the UVPI point spread function. The Institute for Defense Analyses (IDA) generated a number of CHARM 1.3 runs [12,13] for each of the UVPI's plume-camera filter bandpasses observing the Antares plume.

In all of IDA's runs, a 5 by 5 m pixel resolution was used with an aspect angle of 90°. The CHARM 1.3 predictions were convolved with an estimate of the UVPI's PSF. A normalized version of the ground-beacon image, Frame 12778, Orbit 1173, was used as the best UVPI plume-camera PSF estimate. The PSF results in about a 90-m full-width-half-maximum (FWHM) resolution.

Figure 22 is an example of the CHARM 1.3 prediction convolved with the UVPI point spread function. The left image in Fig. 22 shows a false-color CHARM 1.3 image prediction with 5-m resolution, assuming it is being observed with filter PC-4. The right image shows the same CHARM 1.3 prediction but convolved with the UVPI point spread function. Figure 23 is the corresponding contour plot for the convolved image prediction, again using PC-4. Figure 24 shows the corresponding measured contour plot. The measured contour plot and that produced by the predicted plume image convolved with the PSF compare quite closely after rotation to coincide with each other.

The effect on the peak pixel radiance is best illustrated by examining the predicted axial profiles of plume radiance before and after convolution with the PSF. Figures 25 through 28 show examples of predictions before and after convolution. Clearly, these sharply peaked predictions are reduced significantly by the PSF. The more sharply peaked predictions in Figs. 25 and 26 are reduced more, approximately 9:1, than the less sharply peaked predictions of Figs. 27 and 28, approximately 6:1. Table 23 summarizes the peak pixel radiances before and after convolution with the PSF for the data intervals associated with a rocket plume observation. The reduction ratios are also given.

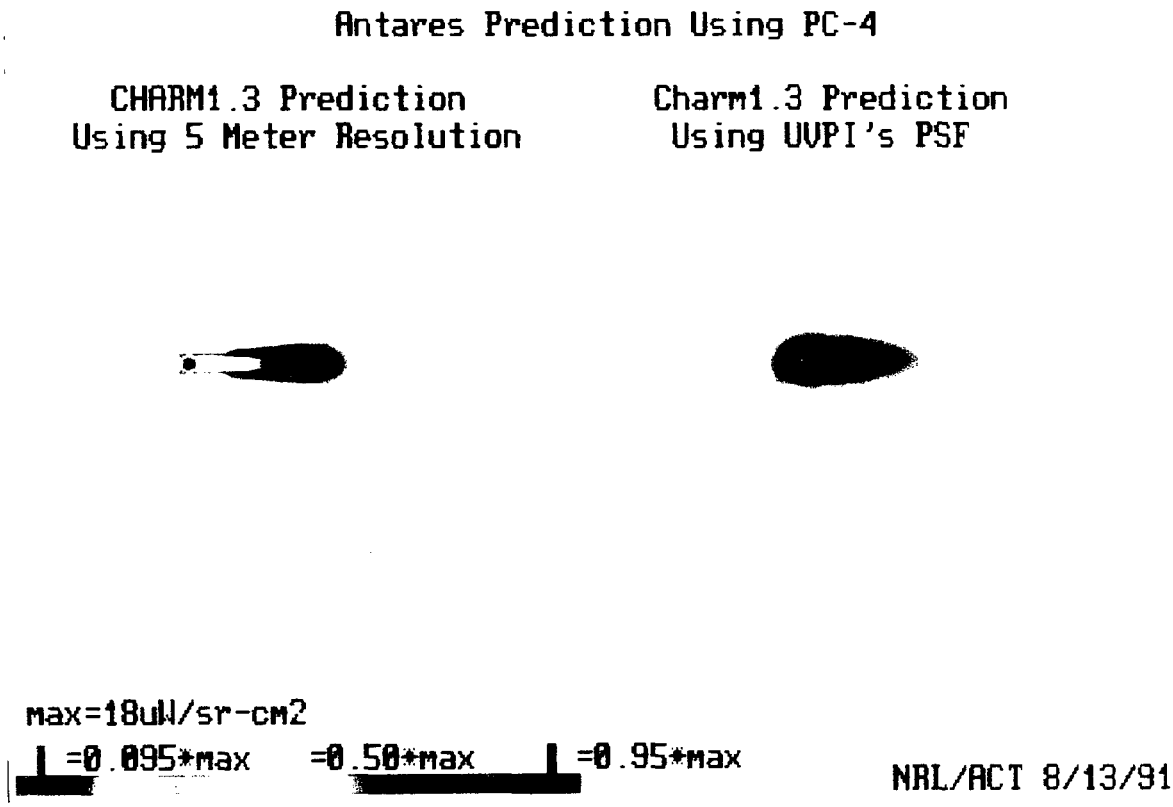

Fig. 22 - PSF convolved CHARM 1.3 plume image using PC-4

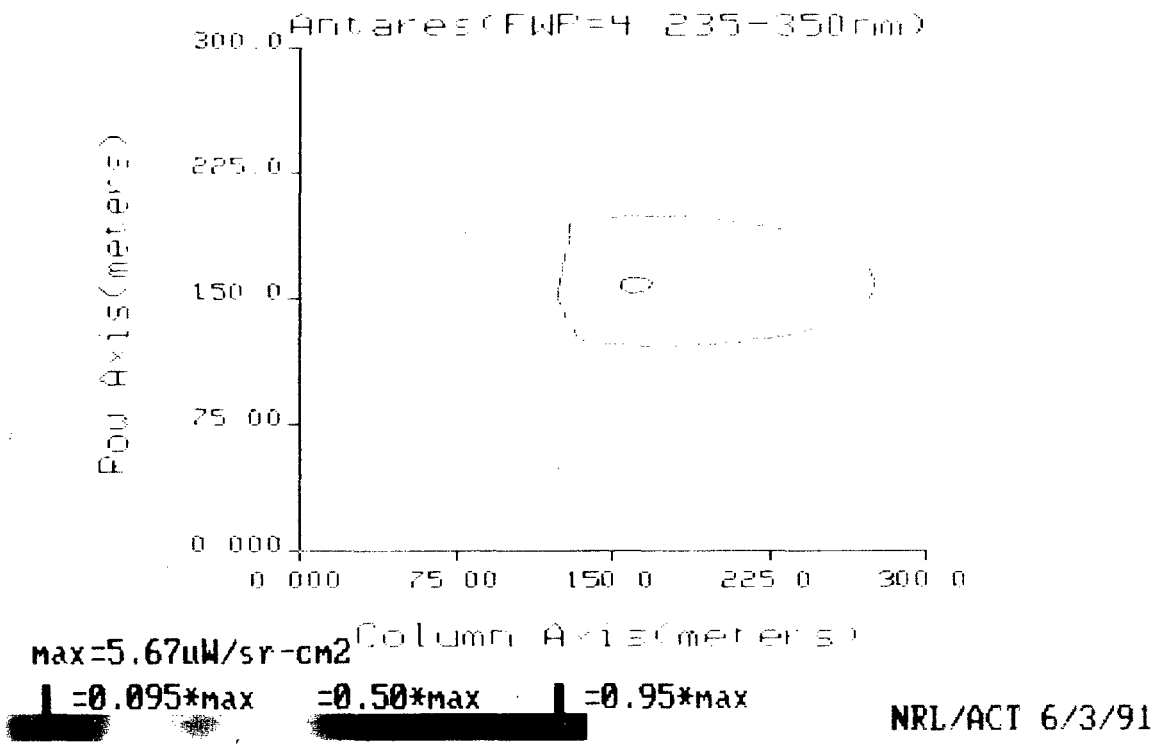

Fig. 23 - PSF convolved CHARM 1.3 contour plot prediction

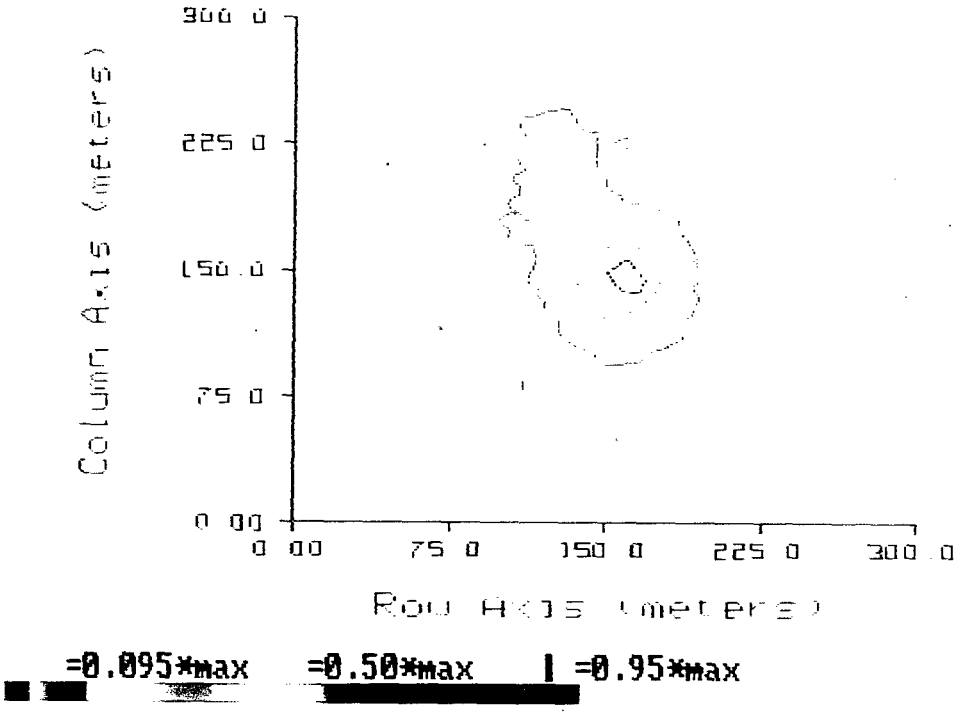

Fig. 24 - Plume-camera contour plot

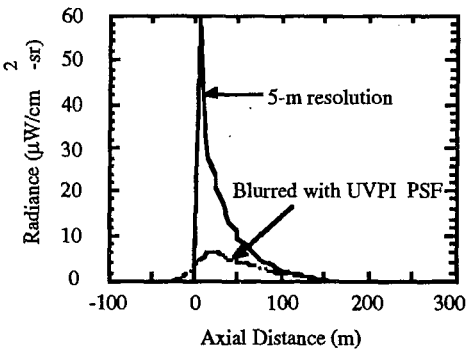

Fig. 25 - CHARM 1.3 predicted and blurred plume axial profile for interval 1

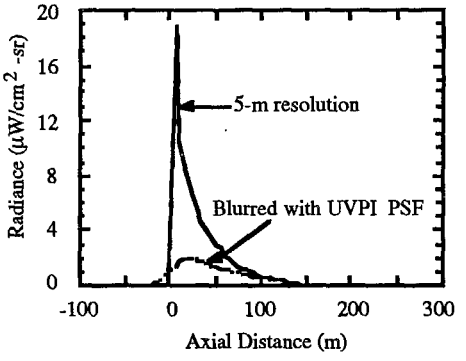

Fig. 26 - CHARM 1.3 predicted and blurred plume axial profile for interval 2

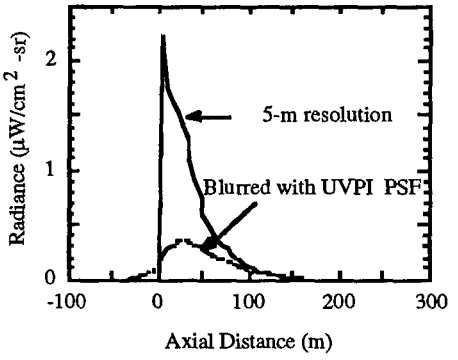

Fig. 27 - CHARM 1.3 predicted and blurred plume axial profile for interval 3

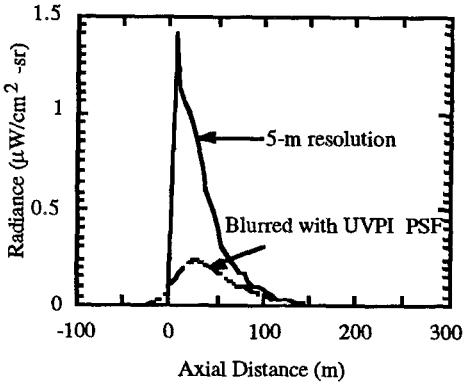

Fig. 28 - CHARM 1.3 predicted and blurred plume axial profile for interval 4

Table 23 - Peak Radiance Comparison

Filter	CHARM 1.3 @ 5-m Resolution Peak Radiance ($\mu W/sr\text{-}cm^2$)	CHARM 1.3 Convolved Peak Radiance ($\mu W/sr\text{-}cm^2$)	Reduction Ratio
PC-4	61.50	6.3	9.8
PC-3	5.28	0.52	10.1
PC-2	11.98	1.3	9.2
PC-1	18.9	2.0	9.5
PC-1	2.21	0.36	6.1
PC-2	1.42	0.23	6.2
PC-3	0.583	0.09	6.5

6.0 RED LEAKAGE

Some sources observed by the UVPI, such as rocket plumes, are much brighter in the visible and near-infrared wavelengths than in the ultraviolet. Therefore, even a strongly attenuated sensitivity to these longer wavelengths may not prevent a significant out-of-band response. An estimate of this out-of-band response requires net quantum efficiency values for the longer wavelengths. Then, calculations of the long wavelength contribution can be made for various assumed input spectra.

6.1 Extended Response

Combinations of very conservative estimates and laboratory measurements were made to define the response of the UVPI into the visible and near-infrared, and the results are shown in this section. It is emphasized that the values presented here are worst-case estimates and represent an upper bound on the long-wavelength response of UVPI.

The estimated worst-case net quantum efficiency extended to long wavelengths for the plume camera is shown in Figs. 29 through 32 plotted on a logarithmic scale. Similarly, the estimated worst-case net quantum efficiency for the tracker camera is shown in Fig. 33.

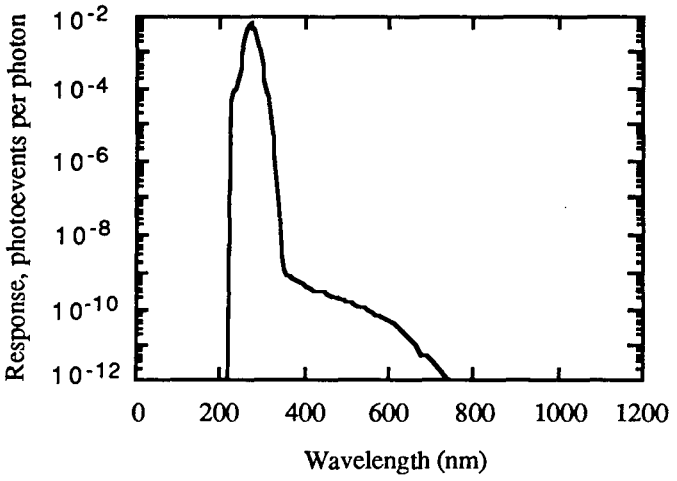

Fig. 29 - Plume camera - extended net quantum efficiency, filter 1

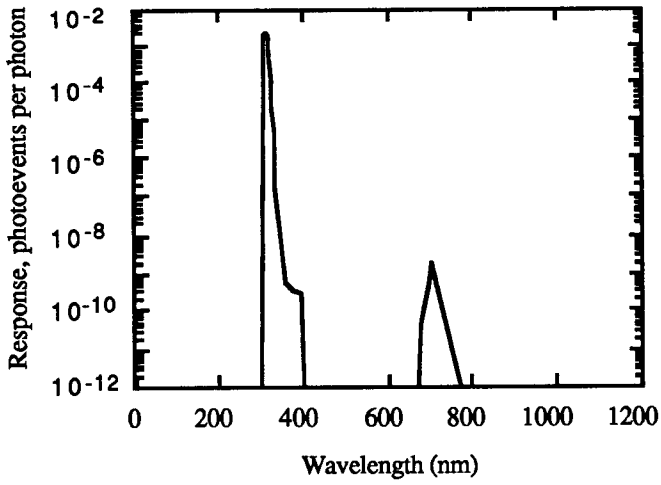

Fig. 30 - Plume camera - extended net quantum efficiency, filter 2

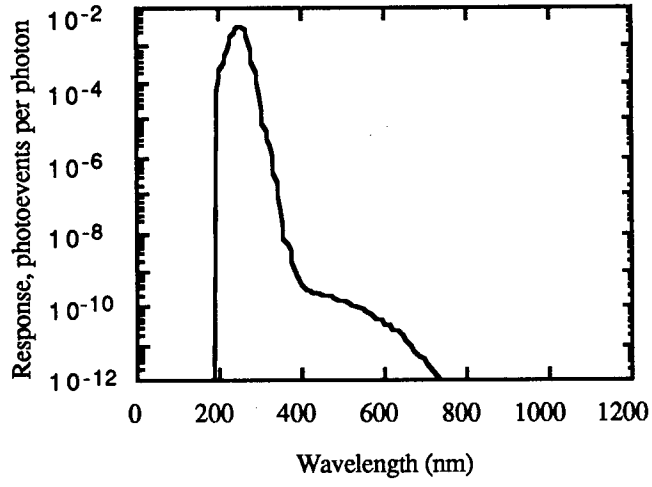

Fig. 31 - Plume camera - extended net quantum efficiency, filter 3

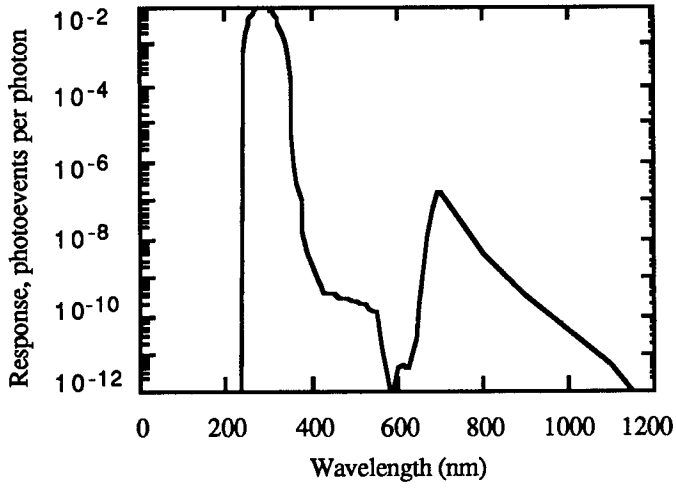

Fig. 32 - Plume camera - extended net quantum efficiency, filter 4

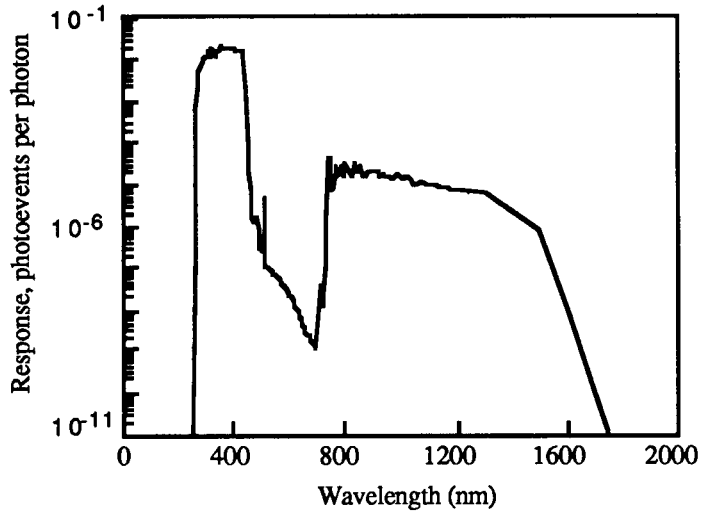

Fig. 33 - Tracker camera - extended net quantum efficiency

6.2 Out-of-Band Response for Several Assumed Spectra

To estimate the possible effects of long-wavelength response, especially for a continuum source like a blackbody, analysis was carried out to determine the percentage of photoevents detected by UVPI that would arise from wavelengths longer than the nominal bandpasses presented in Table 2. This analysis uses the worst-case estimates for long-wavelength response described in the previous paragraphs. The analysis shows that, for the reference spectrum, less than 1% of the photoevents recorded by the plume camera arise from long-wavelength radiation, as seen in Table 24. For the tracker camera, using the same spectral assumptions, no more than 18% of the photoevents arise from red leakage.

Table 24 - Percent Red Leak

	PC-1 (%)	PC-2 (%)	PC-3 (%)	PC-4 (%)	Tracker (%)
Flat spectrum	0.00	0.00	0.00	0.004	0.90
Reference spectrum	0.01	0.04	0.01	0.38	18.0
Blackbody 2300 K	0.06	1.34	0.26	10.8	57.7

7.0 NOISE, SENSITIVITY, AND ERROR ANALYSIS

7.1 Measurement Noise

Measurement noise is usually dominated by photon shot noise statistics. Under certain conditions however, noise in the dark level also becomes significant. (This dark-level noise is intrinsic to the detector and arises from dark current and fluctuations in the baseline of the analog video voltage input to the analog-to-digital converters.) See Section 2.1 for discussion of dark level. Sometimes the noise in the dark field is referred to as read noise.

Based on extensive examination of star measurement data, the signal-dependent noise σ_s can be expressed in terms of the mean number of signal-related photoevents by using the equation:

$$\sigma_s = 2 \bullet \sqrt{P_k}, \tag{17}$$

where P_k is the mean number of signal-related photoevents collected in the kth pixel during the exposure time for an image.

Note that this is about two times the photon shot noise prediction. Figure 34 shows noise in plume-camera star measurements as a function of mean photoevents.

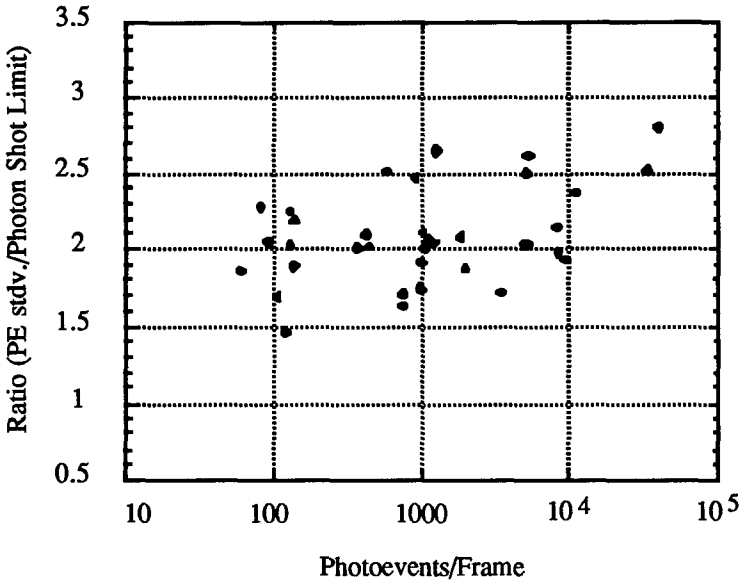

Fig. 34 - Noise in plume-camera star measurements

The total noise standard deviation per image σ_T is given by

$$\sigma_t = \sqrt{\sigma_s^2 + \sigma_I^2}, \tag{18}$$

where σ_I is the signal-independent noise standard deviation for a single pixel due to dark level noise, expressed in photoevents/image. When expressed in DN, this noise source is constant. When expressed in photoevents/image, it depends on the camera gain setting used. This number is empirically determined for each pass and was discussed briefly in Section 2.1.

The total noise standard deviation for M images σ_T is

$$\sigma_T = \sqrt{M \bullet \left(\sigma_s^2 + \sigma_I^2\right)}. \tag{19}$$

Equation (19) requires that P_k be relatively constant for the M images. This will be sufficient for noise-equivalent radiance calculations in the next section, but, in general, the signal will be changing as a function of time and a more general approach, such as the one described in Section 7.3, will be used.

7.2 Instrument Sensitivity

Following the noise-equivalent radiance (NER) definition given in the *Infrared Handbook* [14], the UVPI NER is defined as the source radiance level that will result in a signal-to-noise ratio of 1. It was calculated here for a single pixel only. The NER can be interpreted as the sensitivity limit for one pixel of the imaging system. For UVPI, a single NER number is not sufficient to characterize the sensitivity of the system because sensitivity is a function of exposure time per image, spectral filter,

intensifier gain level, number of images superposed, number of pixels combined spatially, and the assumed source spectrum.

Reference 15 provides a theoretical expression for the signal-power to noise-power ratio applicable to the microchannel plate image intensifier of the UVPI. A single pixel in the plume or tracker camera can be treated as a photoevent counting device. The signal-to-noise ratio (SNR) definition from which the empirical NER can be derived is:

$$(SNR)^2 = M^2 \bullet P_k^2 / \left(M \bullet \sigma_s^2 + M \bullet \sigma_I^2\right), \tag{20}$$

where M, σ_S, σ_I, and P_k have the same meaning as in the previous section.

From this SNR expression, it can be shown that the mean number of signal-related photoevents/image in a pixel that will result in a SNR of 1 is given by:

$$P_k^* = 2\left[1+\left(1+M \bullet \sigma_I^2/4\right)^{1/2}\right]/M. \tag{21}$$

For the case of only one superposed image (M=1) and a negligible level of sensor noise σ_I, the resulting sensitivity limit is 4 photoevents/image, as seen in Table 25. Also, note that the sensitivity improves as a linear function of $1/M$ if the sensor noise is negligible.

The NER is related to P_k^* by a multiplicative constant C, i.e.,

$$NER = C \bullet P_k^* = 2C\left[1+\left(1+M \bullet \sigma_I^2/4\right)^{1/2}\right]/M, \tag{22}$$

where C is the radiometric calibration constant that converts from photoevents/image to W/sr-cm^2. C is a function of the spectral filter used, the single image exposure time, and the assumed source spectrum. Table 26 summarizes the estimated NERs for the plume and tracker cameras for each gain level and filter at an exposure time of $^1/_{30}$th second. The reference spectral shape for rocket plumes was assumed in deriving these NER values.

The radiometric sensitivity can be improved linearly by combining pixels spatially, i.e., performing spatial averaging. In the extreme case of combining all 65,000 pixels, the sensitivity of the entire camera used as a photometer is obtained.

7.3 Errors in Measured Data

The complete estimate of the error in determining radiometric values from the digital numbers reported by the UVPI cameras observing a rocket plume is composed of two components: (a) error due to measurement noise (addressed in Section 7.3.1), which includes photon shot noise and other intrinsic sensor noise sources, and (b) calibration error (discussed earlier in Section 2), which is incorporated into calculation of the total error discussed in Section 7.3.2.

7.3.1 *Calculation of Errors for a Changing Intensity*

In general, for a plume radiant intensity that changes as a function of time, the number of photoevents and, consequently, the photon shot noise, will change as a function of time. Since most rocket thrust curves have a slow variation with time, the plume radiance can be assumed to be constant over a short time interval, i.e., the radiant intensity statistics are not affected by a small shift in time. Thus, a sliding box average for a window of N consecutive images centered about the ith image can be used. Typically, a window size of 15 consecutive images is selected for the statistical analysis of the plume-camera data, and a window of 9 consecutive images is selected for the tracker-camera analysis. A larger time window could be used, with the risk of making invalid the assumption of temporal constancy.

Table 25 - Noise-Equivalent Photoevents Per Pixel for Single Images

Gain Step	Tracker Camera		Plume Camera	
	Photoevents (Per image-pixel)	Photoevents (Per s-pixel)	Photoevents (Per image-pixel)	Photoevents (Per s-pixel)
0	1187.0	35610	48.2	1448
1	618.4	18554	35.6	1070
2	287.4	8622	20.5	618
3	137.2	4116	14.0	423
4	66.7	2003	9.6	290
5	30.5	918	5.9	178
6	16.9	508	4.3	132
7	10.3	310	4.0	122
8	6.2	187	4.0	120
9	4.7	143	4.0	120
10	4.2	127	4.0	120
11	4.0	122	4.0	120
12	4.0	120	4.0	120
13	4.0	120	4.0	120
14	4.0	120	4.0	120
15	4.0	120	4.0	120

Table 26 - Noise-Equivalent Radiance Per Pixel

Gain Step	Tracker ($\mu W/sr\text{-}cm^2$)	PC-1 ($\mu W/sr\text{-}cm^2$)	PC-2 ($\mu W/sr\text{-}cm^2$)	PC-3 ($\mu W/sr\text{-}cm^2$)	PC-4 ($\mu W/sr\text{-}cm^2$)
0	0.590	15.0	94.2	197	27.4
1	0.307	111.0	69.6	145	20.2
2	0.143	63.9	40.2	83.9	11.7
3	0.0682	43.7	27.5	57.4	7.99
4	0.0332	30.0	18.9	39.4	5.48
5	0.0152	18.5	11.6	24.2	3.37
6	0.00842	13.6	8.57	17.9	2.49
7	0.00514	12.7	7.95	16.6	2.31
8	0.00310	12.5	7.84	16.4	2.28
9	0.00237	12.4	7.82	16.3	2.27
10	0.00210	12.4	7.81	16.3	2.27
11	0.00201	12.4	7.81	16.3	2.27
12	0.00199	12.4	7.81	16.3	2.27
13	0.00199	12.4	7.81	16.3	2.27
14	0.00199	12.4	7.81	16.3	2.27
15	0.00199	12.4	7.81	16.3	2.27

Given the number of photoevents as a function of image, the following quantities are defined:

M is number of images in the entire data interval,
N is number of images in the local window,
μ_i is local mean for N images in the window around ith image,
σ_i is local standard deviation for N images in the window around ith image,
ε_i is σ_i/μ_i, local error around the ith image,
ε_N is average local error when using window containing N images,

$$\varepsilon_N = (1/M)\left(\Sigma_i\, \varepsilon_i\right),$$

ε_μ is upper bound error in the measured number for the case of M averaged images,

$$\varepsilon_\mu = \max\left(\varepsilon_i\right)/(M)^{1/2},$$

K is average standard deviation per image normalized with respect to the photon shot noise limit $\sqrt{\mu_i}$,

$$K = (1/N)\Sigma_i\left(\sigma_i/\left(\mu_i\right)^{1/2}\right).$$

To prevent extreme values from affecting the local statistics, the maximum and minimum values within the window were rejected. That is, only N-2 images were used for the local mean and local standard deviation computation.

As an example for the plume camera, Table 27 lists M, the number of images in each data interval, and ε_N, the error due to measurement in the values averaged over the window that consists of N images. The measurements are for the central region of a plume.

Table 27 - Percent Error Per Image Due to Measurement Noise ε_N

Number of Images (M)	Number of Photoevents per Image	K	ε_N (%)
207	16.3	1.29	32.2
157	26.3	1.40	27.8
104	67.7	1.46	17.7

7.3.2 *Total Error for Single and Composite Images*

Assuming that the number of photoevents reported by UVPI and the gain conversion factor G_g are uncorrelated or weakly correlated, then the total error per image ε_F can be obtained from the relation [16]:

$$\varepsilon_F = \left(\varepsilon_N{}^2 \bullet \varepsilon_{1/G}{}^2 + \varepsilon_N{}^2 + \varepsilon_{1/G}{}^2\right)^{1/2}, \tag{23}$$

where ε_N is the average local error in the number of measured photoevents (Table 27) and $\varepsilon_{1/G}$ is the error in the gain conversion factor (Table 28).

Table 28 - Total Percent Error Per Single Image ε_F

$\varepsilon_{1/G}$	ε_N	ε_F
9.9	32.2	33.8
15.9	27.8	32.3
10.5	17.7	20.7

For the case of a composite image composed of M images, an upper bound estimate of the total error is given by

$$\varepsilon_T = \left(\varepsilon_\mu{}^2 \bullet \varepsilon_{1/G}{}^2 + \varepsilon_\mu{}^2 + \varepsilon_{1/G}{}^2\right)^{1/2} . \tag{24}$$

Notice that ε_T can never be smaller than $\varepsilon_{1/G}$, no matter how many images are averaged together.

As an example, Table 29 summarizes the total error ε_T for the central region of a plume observed by UVPI.

Table 29 - Total Percent Error Per Composite Image ε_T

Images (M)	Total Photoevent/S	ε_μ	$\varepsilon_{1/G}$	ε_T
207	3,374	3.6	9.9	10.5
157	4,129	2.9	15.9	16.2
104	7,041	3.3	10.5	11.0

REFERENCES

1. J.T. Wright, "Ultraviolet Plume Instrument (UVPI) Subsystem Users Manual," SDRL 068, Loral EOS Document No. 3731, Loral Electro Optical Systems, Pasadena, CA, Jan. 1989.

2. H.W. Smathers, D.M. Horan, L.H. Reynolds, W. Ramsey, and H.D. Wolpert, "Design and Description of the Ultraviolet Plume Instrument (UVPI)," *Proc. SPIE* **1158**, 196 (1989).

3. H.W. Smathers, G.R. Carruthers, W. Ramsey, G. Steiner, and W. Louissaint, "Calibration and Performance of the Ultraviolet Plume Instrument (UVPI)," *Proc. SPIE* **1158,** 212 (1989).

4. G. Sonneborn, N.A. Oliverson, C.L. Imhoff, R.E. Pitt, and A.V. Holm, "IUE Observing Guide," IUE NASA Newsletter No. 32, p. 1 (1987).

5. A.D. Code, A.V. Holm, and R.L. Bottemiller, "Ultraviolet Photometry from the Orbiting Astronomical Observatory XXXIV, Filter Photometry of 531 Stars of Diverse Types," *Astrophys. J. Suppl.* **43,** 501 (1980).

6. M. Breger, "Catalog of Spectrophotometric Scans of Stars," *Astrophys. J. Suppl.* **32,** 7-87 (1976).

7. C.L. Wyatt, *Radiometric System Design* (Macmillan, New York, 1987).

8. F.E. Nicodemus, "Normalization in Radiometry," *Applied Optics* **12,** 2960-2973 (1973).

9. J. Marqusee, Institute for Defense Analyses, Alexandria, VA, private communication, 14 March 1991.

10. W.A. Jeffrey, Institute for Defense Analyses, M. Slack, and L. Laux, Lockheed Missiles and Space Company. "Orbus Preflight Predictions," IDA document D-755, April 1990.

11. P.W. Erdman, E. Zipf, P. Espy, C. Howlett, D.A. Levin, and G.V. Candler, "In-Situ Measurements of UV and VUV Radiation from a Rocket Plume and Re-entry Bow Shock, " AIAA paper No. 92-0124, Jan 1992.

12. "Experiment Requirements Document for UVPI Observations of Strypi XI," W. Jeffrey, Institute for Defense Analyses, and R. R. Strunce, Jr., Star Technologies Corporation, Feb. 1991.

13. "Radiometric Calculations for Strypi Mission," Memorandum to H.W. Smathers, NRL, from W. Jeffrey, Institute for Defense Analyses, Alexandria, VA, 31 May 1991.

14. W.L. Wolfe and G.J. Zissis, eds., *The Infrared Handbook* (Environmental Research Institute of Michigan, 1978).

15. R.H. Kingston, *Detection of Optical and Infrared Radiation* (Springer-Verlag, New York, 1978), pp 43-51.

16. A. Papoulis, *Probability, Random Variables, and Stochastic Processes,* 2nd ed. (McGraw Hill, New York, 1984).

Appendix A
THE ULTRAVIOLET PLUME INSTRUMENT

A.1.0 UVPI DESCRIPTION AND BLOCK DIAGRAM

The Ultraviolet Plume Instrument (UVPI), designed and built by Loral Electro Optical Systems [A1, A2], comprises six subassemblies (Fig. A1) ranging in size from 4.4 to 0.3 ft^3. The six subassemblies are sensor head assembly, electronics interface assembly, camera frame controller, digital tape recorder, power supply, and tracker assembly. The total weight is about 170 lb, and the operating power consumption averages about 170 W.

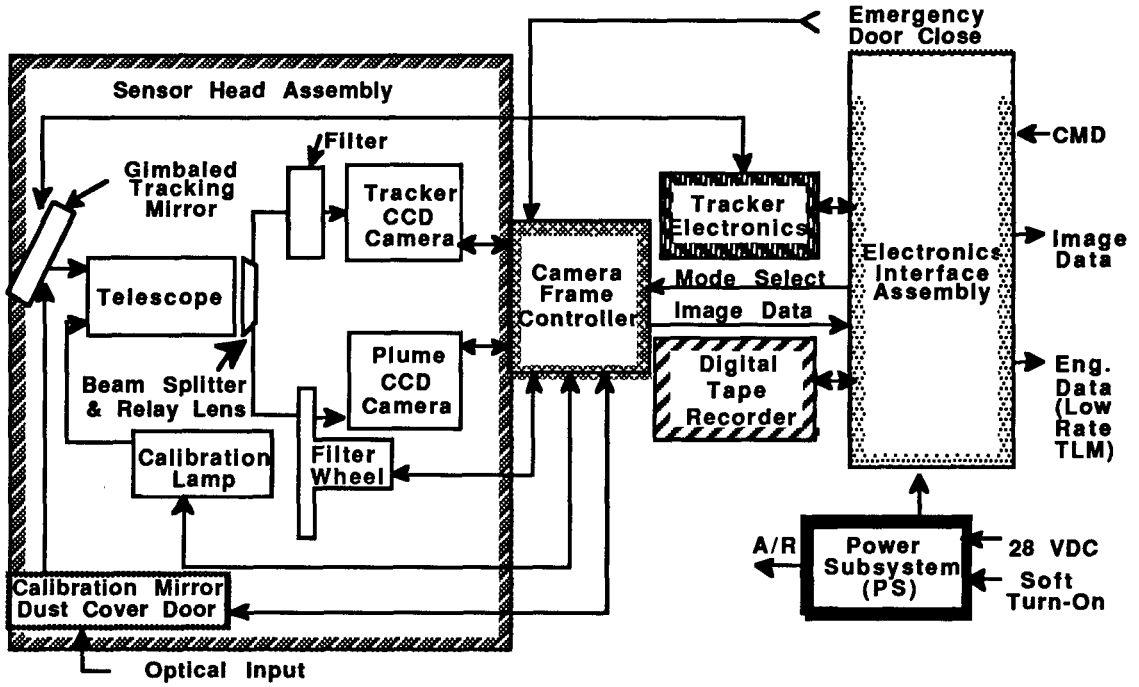

Fig. A1 - UVPI block diagram

There are two intensified charge-coupled-device (ICCD) cameras, the tracker camera and the plume camera, which are boresighted and share a common optical telescope. The tracker camera is used to locate, acquire, and track a target; the plume camera collects target images in the near and mid-ultraviolet wavelengths. The camera images are digitized and transmitted to the ground or are recorded onboard for later transmission. Figure A2 is a diagram of the flow of commands and data within the UVPI.

The instrument was designed to transmit or store images in a selectable normal or high image rate mode because of the limited telemetry data rate, 3.125 Mbps. In the high image rate, or zoom mode, only the central portion of the image is retained. This allows a 30 Hz image rate while using the same bandwidth. The normal image transmission rate is 5 Hz. The photometric range and sensitivity of the UVPI cameras were selected for nighttime operations. That is, the UVPI was designed to view and track relatively bright targets against a dark background.

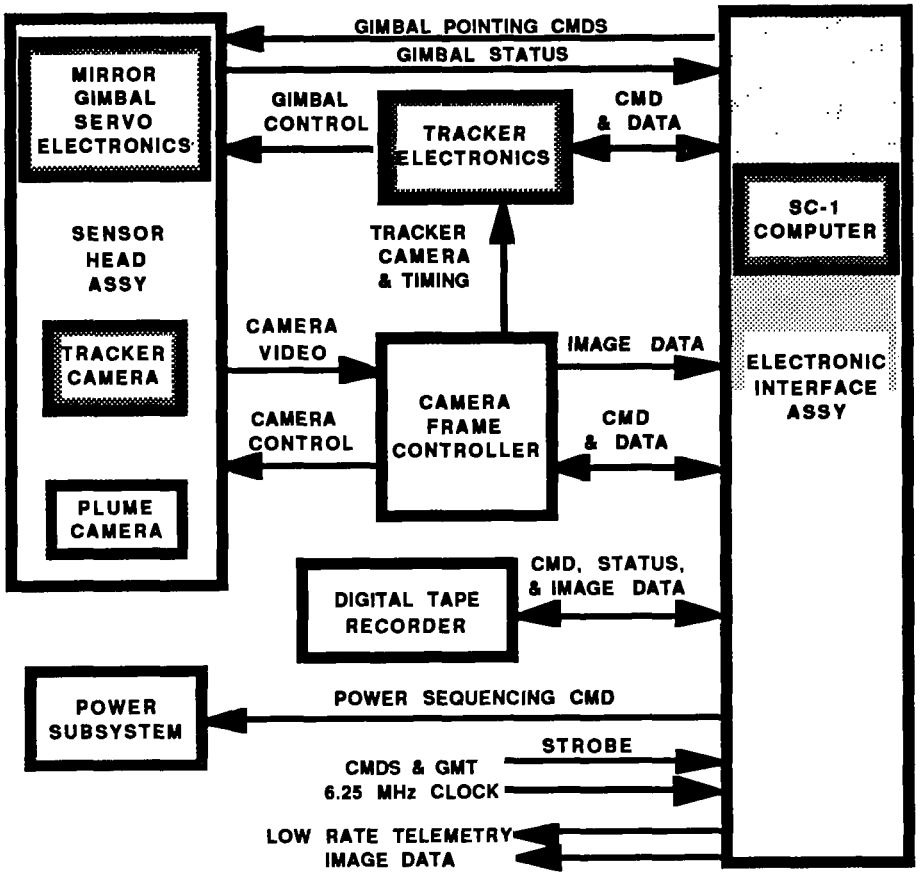

Fig. A2 - Command and data flow within the UVPI

The UVPI is mounted within the satellite and looks through an aperture in the Earth-oriented panel. A gimbaled mirror provides UVPI with a field of regard of a 50° half-angle cone about the satellite's nadir. When the UVPI is not in use, a door covers the aperture. Attached to the inside of this door is a flat mirror that allows the UVPI cameras to view celestial objects or the Earth's limb when the door is partially opened.

A.2.0 SENSOR HEAD ASSEMBLY

The sensor head assembly shown in Fig. A3 houses the UVPI optical components and the two intensified video cameras. The two major sections are the optical bench and the gimbal frame. The optical bench contains the telescope, calibration lamp, tracker and plume cameras, power regulator, filter wheel for the plume camera, filter drive motor, plume-camera folding mirror, relay optics, beam splitter, and the filter for the tracker camera. The optical bench is attached to the gimbal frame that also accommodates the gimbals and resolvers, gimbaled mirror, gimbal caging mechanism, calibration mirror, the door, and the door drive motor.

The telescope shown in Fig. A4 is a Cassegrain configuration with refractor corrector plate. The circular aperture is 10 cm in diameter, yielding 78 cm^2 gross collecting area. A beam splitter allows the two cameras to share the beam and the forward telescope optics. The effective collecting area, which accounts for beam reduction caused by central blocking and the beam splitter, is used in calculating the net quantum efficiency. The focal length for the tracker camera is 60 cm, which gives an f number of 6 and a field of view of 2.60° by 1.98° The plume camera uses a relay lens of

magnification 10.3, which provides a focal length of 600 cm, an *f* number of 60, and a field of view of .184° by .137°.

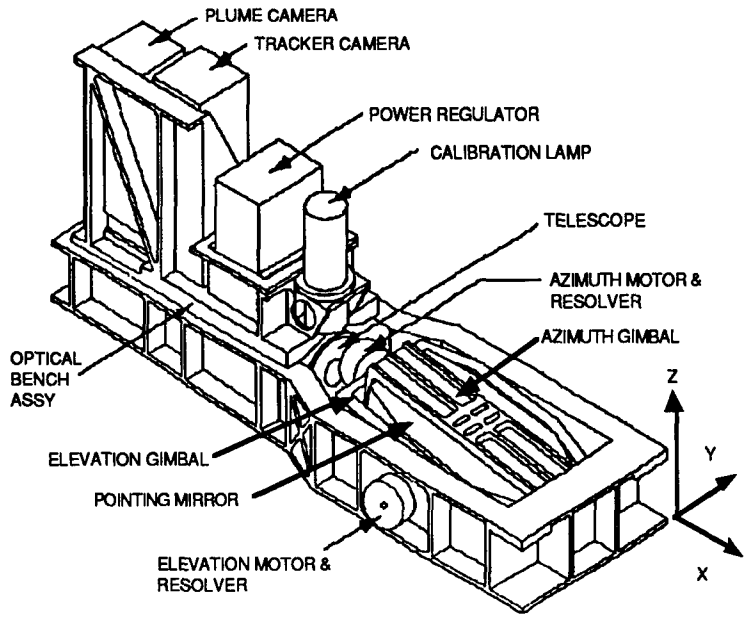

Fig. A3 - UVPI sensor head assembly diagram

The intensified cameras shown in Fig. A5 consist of an image intensifier followed by a fiber-optic reducer and a CCD television camera. The intensifiers, which were made by ITT, convert incoming ultraviolet photons into outgoing green photons, giving a large increase in intensity while preserving the spatial characteristics of the image.

The intensifier is a vacuum-sealed cylinder containing circular quartz windows in front and back. The photocathode material, which converts incoming ultraviolet photons to electrons, is a semi-transparent coating on the inside of the front window. The P20 phosphor, which converts electrons to green photons, is a coating on the inside of the back window. The electrons are multiplied as they pass from front to back through a dual-chevron microchannel plate (MCP) that has electron gains of approximately 10^5 at high gain settings. The electron energy is increased by the phosphor's anode potential. The overall net gain provides about 10^7 green photons per ultraviolet photon.

The tapered fiber optic provides a size reduction of the image to match the intensifier output to the CCD chip input. The CCD chip is a Texas Instrument 241C with a well-transfer function of 1.2 microvolts/electron.

A.3.0 CAMERA FRAME CONTROLLER

The primary function of the UVPI Camera Frame Controller (CFC) is to receive RS-170 video signals from the plume and tracker cameras, digitize them, and supply them to the electronics interface assembly. The received analog video signals are restored, multiplexed, digitized, and summed by internal CFC circuits. The tracker camera's video signal is buffered and made available to the tracker electronics for target centroid calculations and for determination of the gimbaled mirror pointing commands. Camera telemetry data from the CFC and engineering telemetry data from the electronics interface assembly are added to the digitized video frames and telemetered by the LACE spacecraft for later analysis.

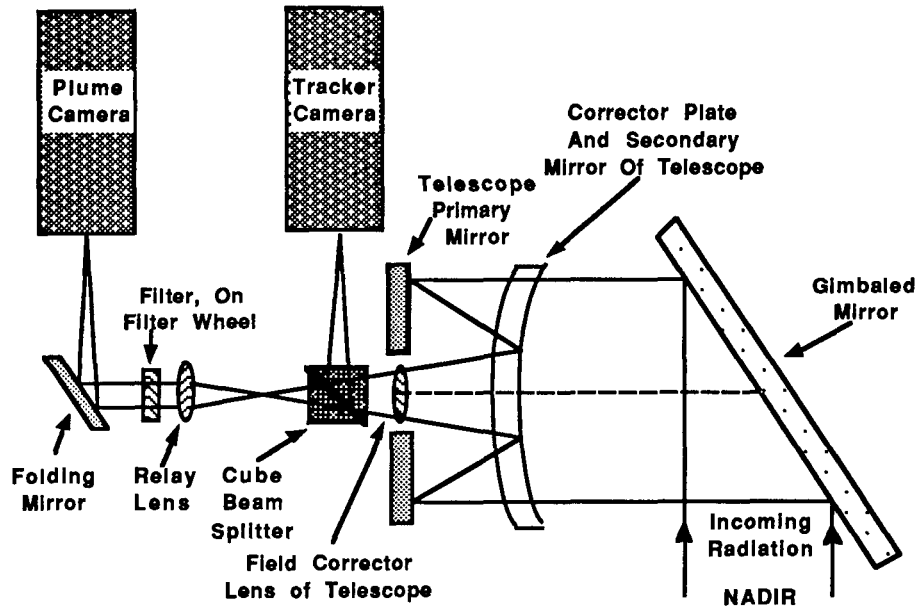

Fig. A4 - UVPI sensor head assembly optics

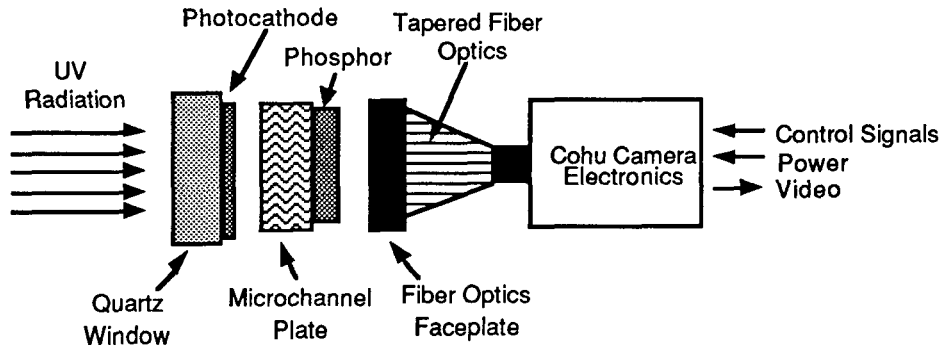

ITT Image Intensifier

- Photocathode
  - CsTe (plume) - 25 mm dia.
  - Bialkali (tracker) - 40 mm dia.
- Microchannel plate
  - 2 Stage (plume)
  - 2 Stage (tracker)
- P 20 phosphor output

Cohu Camera Characteristics

- RS-170 output - 30 frames/s
- 754 pixel x 240 line array [TI 241 chip set]
- Array has 11-mm diagonal

Control - Telemetry

- MCP Gain
- Camera Temperature

Fig. A5 - Schematic of intensified CCD camera

The secondary functions of the CFC are automatic gain control of the exposure of each camera, normal/zoom image rate selection, plume-to-tracker ratio selection, camera telemetry data generation for post-mission reconstruction of the acquired images, filter wheel control, door position control, calibration lamp on/off control, gimbal cage/uncage control, and providing telemetry status data to the electronics interface assembly.

Horizontal and vertical control signals are supplied to both cameras by the CFC for synchronization. An on-board microcontroller allows communication with the electronics interface assembly for receiving commands and periodically sending status information.

The CFC camera frame and field definitions are shown in Fig. A6. The focal plane for each camera is an array of 754 vertical by 480 horizontal pixels. Each video frame is composed of two 754 by 240 pixel fields. The fields from the tracker camera are sent to the tracker electronics at a 60 Hz rate. To form plume- or tracker-camera images for telemetering or onboard storage, three pixels are averaged to form a superpixel, and two fields are then averaged. The result is the 251 vertical by 240 horizontal array of pixels at 30 Hz.

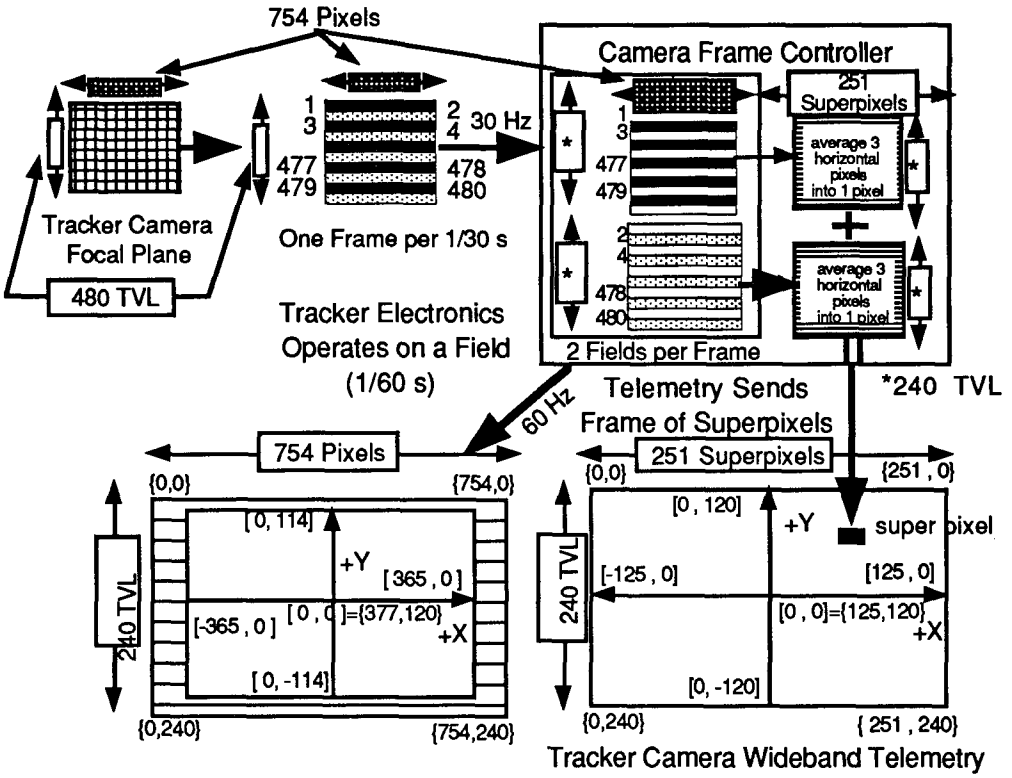

Fig. A6 - UVPI camera frame and field definitions

A.4.0 ELECTRONICS INTERFACE ASSEMBLY

The electronics interface assembly (EIA) is the UVPI system controller. Its function is to receive commands and timing information from the spacecraft and distribute reformatted command and timing to the UVPI subsystems. In addition, the EIA collects video camera data from both cameras and status information from the subsystems for delivery to the high and low speed telemetry spacecraft ports.

The heart of the EIA is the SC-1 control computer, also referred to as the instrument control computer (ICC). This is an environmentally ruggedized, general-purpose, 16-bit computer based on a common 8086-type processor. The computer is fabricated in CMOS, and operates at a 5 MHz clock rate.

The SC-1 provides two main on-board input and output links. The first is a serial data channel, RS-232 format, which communicates with the tracker electronics. This interface is software configurable and operates at a 9600-baud data rate. The second link is an extension of the main CPU bus of the SC-1 and is used for communication within the electronics interface assembly.

Pointing the gimbaled mirror is possible in either open-loop or closed-loop modes. In the open-loop mode, the SC-1 computer uses a pointing function to calculate a sequence of desired azimuth and elevation angles for the gimbals. The gimbal servo then adjusts the gimbal until the

gimbal angle readouts match the desired angles. The pointing function, which calculates the desired angles, consists of two segmented polynomials, each of the same order ranging from three to six. Up to 255 pointing functions can be transmitted and stored in the SC-1 computer, and the desired function can be selected by command.

In the closed-loop mode, the tracker electronics determine the tracking error by measuring the angular displacement between a target centroid and the center of the tracker-camera's field of view. The gimbaled mirror is then moved under control of the tracker electronics to bring the target centroid to the center of the tracker camera's field of view.

The open-loop pointing is used in the POINT mission mode shown in Fig. A7. This mode is used to move the mirror through a scan pattern in order to find the target if it is beyond the tracker-camera's field of view. Once the target is seen in the tracker camera by the ground station operator, the ACQUIRE mode is commanded. This enables the tracker to take control after it has locked onto the target. When this occurs, the mission mode is changed to TRACK. If the target image is lost while it is being tracked, the tracker electronics will enter the EXTRAPOLATE mission mode. Accordingly, the SC-1 computer will point the gimbaled mirror by using a second-order polynomial extrapolation function based on the recent gimbal angle history. If the target reappears during the extrapolated pointing, the tracker electronics will go back into the TRACK mode and regain control of the gimbal.

A.5.0 POWER SUBSYSTEM

The power subsystem provides all of the input power needed by the UVPI at various voltage levels and provides electromagnetic interference protection for the UVPI. To aid LACE's tight power budget, the power subsystem is designed so that lower power levels can be used when mission requirements warrant. This would occur, for example, when only commands are being loaded or when only the tape recorder playback function needs to be actuated. Primary power is received from the LACE spacecraft at 28 volts DC. Maximum power used by the UVPI is 218 W (normal is 157 W).

A.6.0 DIGITAL TAPE RECORDER

The digital tape recorder is a NASA standard magnetic tape recorder used for storing digitized video and engineering data. The unit, designed and manufactured by RCA, can store approximately 7 min of data at 2.7 Mbps.

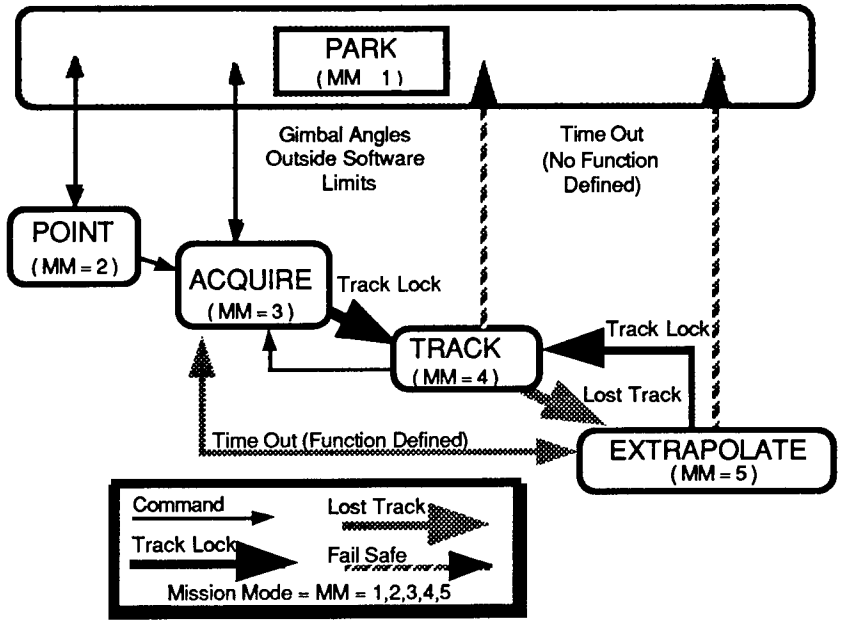

Fig. A7 - Allowable mission mode transitions

A.7.0 UVPI TRACKING SUBSYSTEM

The tracking subsystem specification requirements and performance are listed in Table A1.

Table A1 - Tracking Subsystem Requirements and Performance

Specifications	Requirements	Measured Performance
Position loop bandwidth	5 Hz	5 Hz
Pointing error	400 μrad RMS	96 μrad RMS
Tracking jitter	15 μrad RMS	6 μrad RMS
Tracking velocity	1 deg/s	7 deg/s
Tracking acceleration	0.05 deg/s^2	5 deg/s^2

A.7.1 Tracker Camera

The UVPI is mounted within the satellite and looks through an aperture in the Earth-oriented panel. By using a gimbaled mirror, the UVPI has a field of regard (FOR) of a 50° half-angle cone about the satellite's nadir (Fig. A8). The tracker camera's field of view (FOV) is 2.60° by 1.98°, which corresponds to approximately 22 km by 16 km on the ground at nadir. The tracker camera characteristics are given in Section 1.2.

A.7.2 Tracker Electronics

Figure A9 shows the functions of the tracker electronics. The tracker camera's video signal is received from the camera frame controller on a RS-170 link at 60 fields per second. The video signal is first passed through the spot remover that removes the effects of sensor blemishes and optical system obstructions, and removes background clutter on a field-to-field basis. The spot remover contains two video memories to map spot locations. One memory stores the short-term map for background clutter subtraction, and the other memory stores the map of longer lasting blemishes. The correction for blemishes is achieved by substituting a predetermined video level for the blemished location.

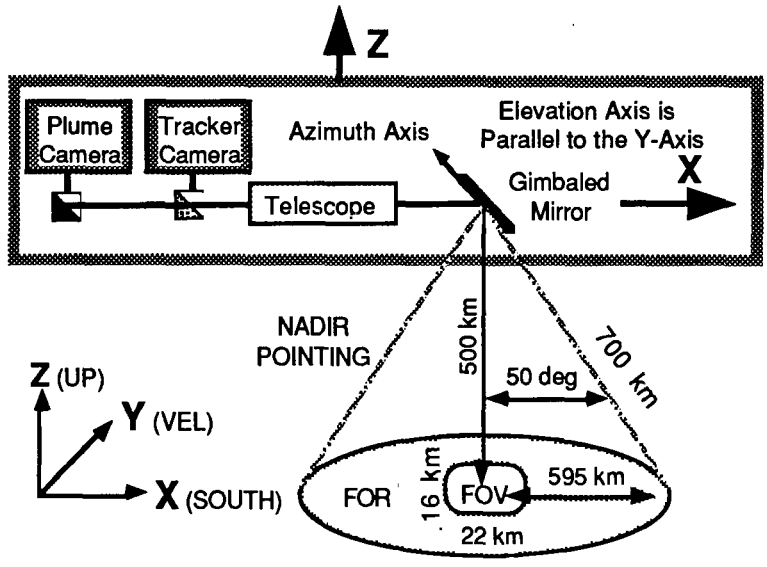

Fig. A8 - Tracker-camera FOV and FOR

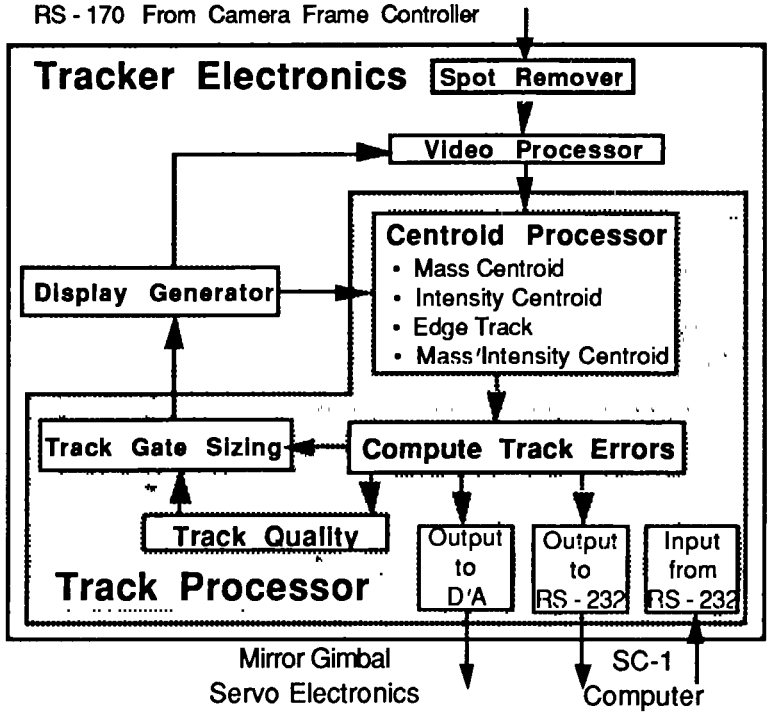

Fig. A9 - Functions of tracker electronics

After passing through the spot remover, the video signal enters the video processor. The video processor also receives the horizontal and vertical control signals and a clock signal to control synchronization and data sampling. The video processor also determines the target size.

A tracking window, or track gate, bounds the subarray of pixels that are identified as part of the target. The size of the tracking window can be directly controlled by the SC-1 computer or by the track gate sizing portion of the tracker electronics as a ratio with the target size.

The data from the pixels within the tracking window are sent to the centroid processor, which can use one of several algorithms to determine the location of the target in the tracker camera's focal plane.

Algorithm choices include mass centroid, which spatially averages all pixels above threshold with equal weighting; intensity centroid, which weights each pixel by the intensity of its response; and mass and intensity centroid. For mass and intensity centroid tracking, the intensity centroid algorithm is used to determine the target position within the field of view and the mass centroid algorithm is used to calculate the target size and target validity.

Figure A10 shows the definitions associated with the tracker camera's focal plane that the tracker electronics use in determining the target location in the focal plane. The tracking error is used to command the gimbal servo electronics to drive the tracking error to zero. The gimbal commands are converted to analog signals and transmitted to the gimbal servo electronics at 60 Hz. The tracker electronics transmits data to the SC-1 computer in a command-response sequence except during the TRACK mode, when the output data are transmitted at 30 Hz.

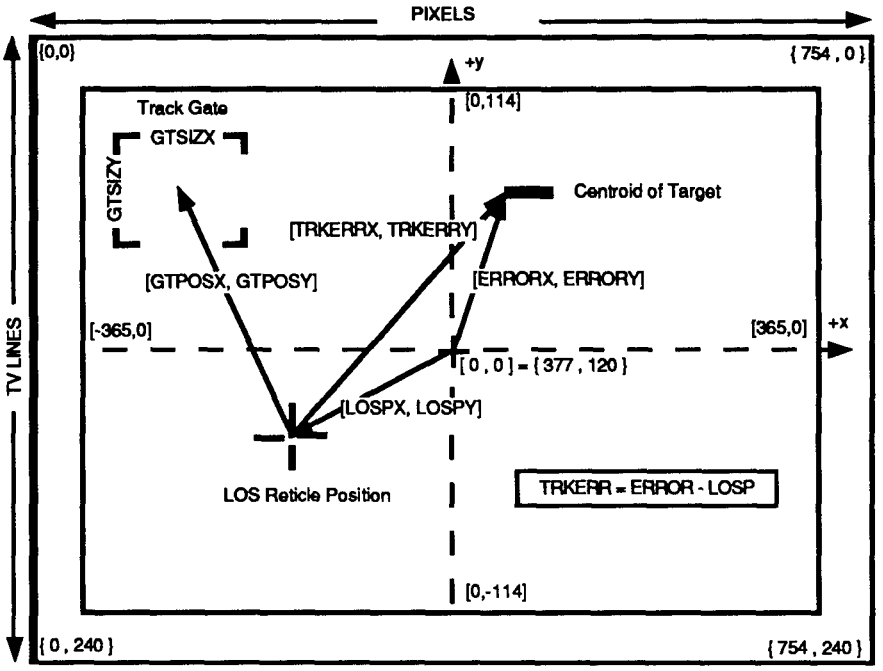

Fig. A10 - Definitions associated with tracker-camera's focal plane

REFERENCES

A1. J.T. Wright, "Ultraviolet Plume Instrument (UVPI) Subsystem Users Manual," SDRL 068, Loral EOS Document No. 3731, Loral Electro Optical Systems, Pasadena, CA, Jan. 1989.

A2. H.W. Smathers, D.M. Horan, L.H. Reynolds, W. Ramsey, and H.D. Wolpert, "Design and Description of the Ultraviolet Plume Instrument (UVPI)," *Proc. SPIE* **1158**, 196 (1989).

GLOSSARY

A/D	analog-to-digital
CCD	charge-coupled device
CFC	camera frame controller
CMOS	complementary metal oxide semiconductor
CPU	central processing unit
DN	digital numbers
EIA	electronics interface assembly
FOR	field of regard
FOV	field of view
FPA	focal plane array
FWHM	full-width-half-maximum
ICC	instrument control computer
ICCD	intensified charge-coupled device
IUE	International Ultraviolet Explorer
LACE	Low-power Atmospheric Compensation Experiment
Mbps	megabits per second
MCP	microchannel plate
MTF	modulation transfer function
NER	noise-equivalent radiance
NRL	Naval Research Laboratory
OAO	Orbiting Astrophysical Observatory
PC-N	plume camera filter, N=1,2,3,4
PE	photoevent
PSF	point spread function
RMS	root-mean-square
SDIO	Strategic Defense Initiative Organization
SNR	signal-to-noise ratio
TALO	time after lift off
UV	ultraviolet
UVPI	Ultraviolet Plume Instrument